Reflection of an acoustic line source by an impedance surface with uniform flow[☆]

E.J. Brambley[a,*], G. Gabard[b]

[a] *Department of Applied Mathematics and Theoretical Physics, University of Cambridge, Wilberforce Road, Cambridge, CB3 0WA, United Kingdom*
[b] *Institute of Sound and Vibration Research, University of Southampton, Highfield, Southampton, SO17 1BJ, United Kingdom*

Abstract

An exact analytic solution is derived for the 2D acoustic pressure field generated by a time-harmonic line mass source located above an impedance surface with uniform grazing flow. Closed-form asymptotic solutions in the far-field are also provided. The analysis is valid for both locally-reacting and nonlocally-reacting impedances, as is demonstrated by analysing a nonlocally reacting effective impedance representing the presence of a thin boundary layer over the surface. The analytic solution may be written in a form suggesting a generalization of the method of images to account for the impedance surface. The line source is found to excite surface waves on the impedance surface, some of which may be leaky waves which contradict the assumption of decay away from the surface predicted in previous analyses of surface waves with flow. The surface waves may be treated either (correctly) as unstable waves or (artificially) as stable waves, enabling comparison with previous numerical or mathematical studies which make either of these assumptions.

The computer code for evaluating the analytic solution and far-field asymptotics is provided in the supplementary material. It is hoped this work will provide a useful benchmark solution for validating 2D numerical acoustic codes.

Keywords: Acoustic line source, impedance lining, method of images, grazing flow.

1. Introduction

Impedance surfaces are an important concept in acoustics, as they can be used to represent the response of any surface to small amplitude perturbations (such as sound or instabilities), and have been successfully employed in applications ranging from outdoor acoustics over a porous ground [2] to acoustic linings in aircraft engine intakes [3]. The mean flow present in aircraft engine intakes complicates the interaction between the acoustics and the impedance surface, potentially allowing for instabilities to grow over the surface [4]. In order to investigate the behaviour of sound interacting with an impedance surface, either plane waves or localized (point or line) sources are usually employed. While plane waves are conceptually simpler, localized sources have two important advantages. Firstly, the solution to a point or line source forcing represents the Green's function, and can therefore be used to construct the response of an impedance surface to arbitrary forcing (including, but not limited to, localized dipole and quadrupole forcing). Secondly, localized sources are far better suited to verifying the correctness of computational acoustic simulations, since they involve no incoming waves from outside the computational domain and since they excite all supported acoustic modes (including possibly unstable surface modes). For these reasons, this paper presents an

[☆] A preliminary version of some parts of this paper was presented as part of AIAA Paper 2013-2218 at the 19th AIAA/CEAS Aeroacoustics Conference in Berlin, Germany [1].

[*] Corresponding author. Tel.: +44 1223 760457. Fax.: +44 1223 765900.
Email addresses: E.J.Brambley@damtp.cam.ac.uk (E.J. Brambley), G.Gabard@soton.ac.uk (G. Gabard)

analytic solution to the simplest possible situation involving a localized source, an impedance surface and a mean flow, this being the 2D situation of a uniform flow over an infinite constant-impedance surface subjected to a harmonic line forcing.

There have been many studies of the behaviour of an infinite flat impedance surface subjected to a point source in 3D [5–10] and subjected to a line source in 2D [11–14]. None of these studies consider a mean flow. Moreover, all of these studies start with a statement that the solution may be written as a sum of a free-field, or direct, wave, and a reflected wave. Integral identities are then manipulated to find a correction to either a hard-walled ($Z = \infty$) or pressure-release ($Z = 0$) reflected wave, or to find the functional form of a reflection coefficient, often involving the manipulation of integrals of Bessel identities and/or the decomposition of cylindrical waves into an integral over plane waves. Here, we use a much simpler and more direct formulation by solving directly the Helmholtz equation using a Fourier transform. The solution derived in this way is naturally found to separate into a direct and a reflected term, and for locally-reacting surfaces the reflected term is naturally of the form of a pressure-release reflection plus a correction.

The classical method of images may be used to compute the reflected wave for a hard-wall or a zero-pressure surface. Morse and Bolt [5, pp. 141–143] found a comparable result for a general impedance surface for a 3D point source, which consisted of an image point source plus an image line source perpendicular to the surface, thus providing a generalization of the method of images. This result has been repeatedly rediscovered, as pointed out by Taraldsen [10], who argued that this image line source is better viewed as a complex line source extending in the imaginary normal direction to the surface. Here, we find a comparable generalization for the reflection of a 2D line source; this generalization of the method of images in 2D is different from the 3D generalization, albeit with certain similarities.

An impedance surface often supports waves itself, which are here referred to as surface waves. For a point source in 3D, Attenborough et al. [7], building on the work of Paul [6], performed a steepest descent analysis and found a pole that gave rise to a surface wave. For a 2D line source, Mechel [14] also found a pole that lead to a surface wave. Here, due to the inclusion of mean flow, the surface wave behaviour is expected to be rather different [4, 15], with one such surface wave potentially corresponding to a hydrodynamic instability of flow over the surface. Due to this complication, Rienstra and Tester [16] choose to neglect the possible instability of the surface waves as an explicit modelling assumption while deriving their Green's function for a 3D point source in a lined cylindrical duct with flow. Studies of surface waves with flow [4, 15, 17] have so far investigated only the propagation of surface waves, and have not consider their generation by an explicit acoustic source. Because of this, these studies assumed the surface waves to be localized to the surface and to decay exponentially away from it, which Crighton [18] showed need not be true if the acoustic source is included in the model. Crighton demonstrated this by showing that flow over an elastic plate subjected to a line source results in "leaky waves" that initially grow exponentially away from the surface before eventually being cut off by a Fresnel region. Here, a similar effect is found.

In addition to providing insight into the nature of the solution, the analysis of a line source above an impedance surface with flow represents a useful benchmark problem against which to validate numerical simulations. Choosing a problem to benchmark against can be difficult. For a realistic situation involving complicated geometries where no exact analytic solution exists, such as a 3D mode propagating out of a realistic aeroengine intake [19], comparisons can only be made against approximate analytic solutions, such as those using the Method of Multiple Scales [20–24]. In such situations, it is unclear how well the analytic and numerical solutions should be expected to match, since the analytic solution is only approximate. Similarly, validating numerical simulations against experimental results, as performed by Richter [19] using the NASA Grazing Incidence Tube experimental results [25], has the disadvantage that the mode excited, the definition of the liner impedance and the measured results are all subject to experimental error, and that moreover the results appear sensitive to other factors such as the tube's downstream exit impedance, 3D effects, and viscous and boundary layer effects [26–28]. Simple test cases therefore allow an exact comparison between the numerical simulation and an analytic solution, one of the simplest of which is that of an oblique plane wave reflecting from an impedance surface [29]; a number of common validations for 2D and 3D time-dependent numerical acoustics simulations with flow are described by Richter [19, chapter 7.1], and similar validations are also used in 2D and 3D frequency-domain simulations [e.g. 30]. However, while these situations are sufficiently simple to permit an exact closed-form analytical expression for the pressure

field, all of these tests rely on accurately introducing an incoming acoustic wave at the boundary of the numerical domain, while many of them also do not test the correct simulation of surface waves, do not test the impedance surface at a range of axial wavelengths, nor test correct propagation to the far field. Here, we consider a simple 2D benchmark problem which avoids all of these limitations, yet which still permit an analytic solution. Apart from the implementation of the impedance boundary condition, this benchmark problem is relatively straightforward to simulate numerically, and does not require the forcing of an incoming wave or mode at a numerical boundary.

In §2, both exact analytical solutions and leading-order asymptotic far-field solutions are derived directly from the governing equations. The results are valid for both locally- and nonlocally-reacting impedance surfaces, and this is demonstrated in §3 by implementing a modified impedance boundary condition [31] which accounts for a thin boundary layer over the impedance surface and results in an effective impedance which is nonlocal. Plots of the results of both of these sections are given in §4, before the implications of the analysis for our understanding of surface waves and the 2D generalization of the method of images are given in §5 and §6 respectively. A summary and a discussion of how the results presented here could be generalized is then given in §7.

2. Analytic and asymptotic solutions

We consider the simplest possible situation involving a localized source, an impedance surface and a mean flow. Specifically, we consider a uniform mean flow of Mach number M flowing in the positive x-direction over an impedance surface occupying the plane $y = 0$, on top of which we introduce a time-harmonic localized source located at $x = 0$ and $y = y_s$. Here, a line mass source is chosen for analytic and computational simplicity, although 2D solutions involving dipoles, quadrupoles, or distributed sources could be deduced directly from this line source analysis. Moreover, while uniform mean flow is considered here, a more realistic sheared boundary layer mean flow may be represented by incorporating the effect of the sheared flow into the impedance of the surface [31–33], as will be demonstrated in §3, provided the source is outside the region of sheared flow. For sources within the sheared flow region, a different analysis would be needed taking account of the sheared flow explicitly [see, e.g., 34–36].

Throughout what follows, we nondimensionalize density by the (constant) mean flow density ρ_0, velocity by the constant sound speed c_0, and distance by an arbitrary length scale a (so that time is nondimensionalized by a/c_0). While it may at first sight seem confusing to nondimensionalize using an arbitrary lengthscale a, here we prefer to keep a arbitrary to aid comparison with previously investigations where a is already specified, such as the radius of a duct or the chord length of a wing[1].

Our governing equations are therefore the Linearized Euler Equations, and eliminating all but the perturbation pressure $\hat{p}$ leads to the convected wave equation

$$\frac{D^2\hat{p}}{Dt^2} - \boldsymbol{\nabla}^2\hat{p} = \frac{DS}{Dt}, \qquad \text{with} \qquad S = \delta(x)\delta(y - y_s)\mathrm{e}^{\mathrm{i}\omega t}, \tag{1}$$

where $D/Dt = \partial/\partial t + M\partial/\partial x$ is the convective derivative with respect to the mean flow, and S is the mass source per unit distance in the z-direction, y_s is the height of the source above the impedance surface, and ω is the Helmholtz number. Since Eq. (1) is linear and the source is time harmonic with time dependence $\exp\{\mathrm{i}\omega t\}$, so too will the solution be time harmonic with the same dependence. It may be noted that, in the absence of an impedance surface, Eq. (1) may be solved using a Lorentz transform and the standard unconvected Green's function in 2D[2]. However, since this is not possible with an impedance surface present (since the Lorentz transform interferes with the impedance surface), we proceed using a more general derivation.

[1] Readers worried by the arbitrary length scale a should take a to be the distance of the source from the impedance surface, and then set $y_s = 1$ in what follows.

[2] Using, for example, the change of variables $\hat{x} = x/\beta$, $\hat{y} = y$, and $\hat{t} = \beta t + Mx/\beta$ with $\beta^2 = 1 - M^2$, the solution to Eq. (1) with no impedance surface is found to be $\hat{p}_{\mathrm{dir}}$ as given in Eq. (16).

For what follows, it will turn out to be helpful to take $\mathrm{Im}(\omega) = -\varepsilon$ with $\varepsilon > 0$, with the solution for real ω being obtained in the limit $\varepsilon \to 0$. Fourier transforming in the x-direction, so that

$$\hat{p}(x, y, t; y_s) = \frac{\mathrm{e}^{\mathrm{i}\omega t}}{2\pi} \int_{-\infty}^{\infty} p(y; k, \omega, y_s) \mathrm{e}^{-\mathrm{i}kx} \, \mathrm{d}k, \tag{2}$$

transforms the governing equation (1) into

$$\frac{\mathrm{d}^2 p}{\mathrm{d}y^2} + \alpha^2 p = -\mathrm{i}(\omega - Mk)\delta(y - y_s), \tag{3}$$

where α is the transverse wavenumber given by

$$\alpha^2 = (\omega - Mk)^2 - k^2, \qquad \text{with } \mathrm{Im}\big(\alpha(k)\big) < 0 \text{ for } k \in \mathbb{R}. \tag{4}$$

The surface $y = 0$ is assumed to behave as an impedance surface; that is, in the absence of mean flow, a pressure $P \exp\{\mathrm{i}\omega t - \mathrm{i}kx\}$ acting on the surface would lead to a vertical velocity $-V \exp\{\mathrm{i}\omega t - \mathrm{i}kx\}$ in the positive y-direction, with the impedance given by $P/V = Z(k, \omega)$. If the motion of the surface at one point is independent of the motion of the surface everywhere else, including neighbouring points on the surface, then the surface is called *locally-reacting*, and in this case Z may depend on the temporal frequency ω but must be independent of the spatial wavenumber k. A general impedance surface with an impedance depending on both ω and k (for example, an elastic membrane or a thin elastic plate [37]) is called *nonlocally-reacting*. Although later a modified impedance boundary condition [31] will be substituted, for now the impedance boundary condition with the mean flow included is taken to be the Myers [38] boundary condition, given by

$$\mathrm{i}\omega Z \frac{\mathrm{d}p}{\mathrm{d}y} + (\omega - Mk)^2 p = 0 \qquad \text{at } y = 0. \tag{5}$$

For the derivations that follow, unless specified explicitly, we allow for both locally and nonlocally reacting surfaces since Z is allowed to be a function of k as well as ω.

Since we have taken $\mathrm{Im}(\omega) < 0$ (which can be thought of as the source growing exponentially in strength), causality requires the radiation boundary condition at infinity that $\hat{p} \to 0$ when $k \in \mathbb{R}$.

2.1. The solution in Fourier space

Discounting solutions which grow exponentially as $y \to \infty$, the solution to Eq. (3) is given by

$$p = \begin{cases} A\mathrm{e}^{-\mathrm{i}\alpha y} & y > y_s, \\ B\sinh(\mathrm{i}\alpha y) + C\cosh(\mathrm{i}\alpha y) & y < y_s. \end{cases} \tag{6}$$

To this solution we must now apply the impedance boundary condition (5) at $y = 0$, and the continuity and jump of derivative conditions at $y = y_s$ dictated by the delta function source term. Doing so gives the solution

$$p = \frac{(\omega - Mk)\mathrm{e}^{-\mathrm{i}\alpha y_>}}{\alpha\big[(\omega - Mk)^2 + \alpha\omega Z\big]} \big[(\omega - Mk)^2 \sinh(\mathrm{i}\alpha y_<) + \alpha\omega Z \cosh(\mathrm{i}\alpha y_<)\big], \tag{7}$$

where $y_> = \max\{y, y_s\}$ and $y_< = \min\{y, y_s\}$, which may be rearranged to give

$$p = \frac{(\omega - Mk)}{2\alpha} \left[\mathrm{e}^{-\mathrm{i}\alpha|y - y_s|} - \frac{(\omega - Mk)^2 - \alpha\omega Z}{(\omega - Mk)^2 + \alpha\omega Z} \mathrm{e}^{-\mathrm{i}\alpha(y + y_s)}\right]. \tag{8}$$

Inverting the Fourier transform and taking each of the two terms in the square brackets separately gives the solution in real space as $\hat{p} = \hat{p}_{\mathrm{dir}} + \hat{p}_{\mathrm{refl}}$, where

$$\hat{p}_{\mathrm{dir}}(x, y, t; y_s) = \mathrm{e}^{\mathrm{i}\omega t} \int_{-\infty}^{\infty} \frac{(\omega - Mk)}{4\pi\alpha} \mathrm{e}^{-\mathrm{i}kx - \mathrm{i}\alpha|y - y_s|} \, \mathrm{d}k, \tag{9a}$$

$$\hat{p}_{\mathrm{refl}}(x, y, t; y_s) = \mathrm{e}^{\mathrm{i}\omega t} \int_{-\infty}^{\infty} \frac{\alpha\omega Z - (\omega - Mk)^2}{\alpha\omega Z + (\omega - Mk)^2} \frac{(\omega - Mk)}{4\pi\alpha} \mathrm{e}^{-\mathrm{i}kx - \mathrm{i}\alpha|y + y_s|} \, \mathrm{d}k. \tag{9b}$$

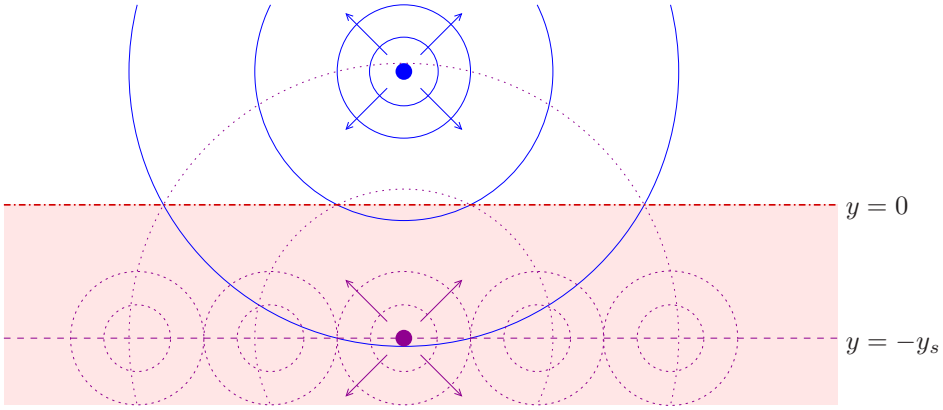

Figure 1: Schematic to show the distribution of image line sources needed along $y = -y_s$ to satisfy the impedance boundary condition at $y = 0$. Solid lines indicate wavefronts from the direct line source $\hat{p}_{\text{dir}}$; dotted lines indicate wave fronts from the distribution of line sources along $y = -y_s$, which combine to give $\hat{p}_{\text{refl}}$; filled circles denote locations of delta function line sources; and the dot-dashed line shows the impedance surface.

The first of these, $\hat{p}_{\text{dir}}$, represents the direct wave due to the mass source in the absence of the impedance surface. The second, $\hat{p}_{\text{refl}}$, represents the effect of reflection by the impedance surface. Note that there are poles of the integrand of $\hat{p}_{\text{refl}}$ given by the solutions of $D(k, \omega) = 0$, where

$$D(k, \omega) \equiv (\omega - Mk)^2 + \alpha(k)\omega Z \tag{10}$$

is exactly the dispersion relation for surface waves at an impedance surface in flow [4]. However, a subtlety that will emerge later is that the branch cut required to be taken for α for non-real k here will turn out to have to be different to that taken by Ref. 4, the interesting implications of which are discussed in §5. Eq. (9b) may be interpreted as giving the reflection $\hat{p}_{\text{refl}}$ as a convolution over a line of image line sources a depth $y = -y_s$ below the surface,

$$\hat{p}_{\text{refl}}(x, y, t; y_s) = \int_{-\infty}^{\infty} \mathcal{R}(x_s)\hat{p}_{\text{dir}}(x - x_s, y, t; -y_s)\,\mathrm{d}x_s, \tag{11}$$

where the generalized reflection coefficient $\mathcal{R}(x)$ is given by

$$\mathcal{R}(x) = \frac{1}{2\pi}\int_{-\infty}^{\infty} \frac{\alpha\omega Z - (\omega - Mk)^2}{\alpha\omega Z + (\omega - Mk)^2} \mathrm{e}^{-\mathrm{i}kx}\,\mathrm{d}k. \tag{12}$$

A schematic of this is given in Fig. 1. Note that $\mathcal{R}(x)$ is independent of y_s, and that Eq. (11) depends on Z only through $\mathcal{R}(x)$, so that all information about the impedance surface is contained within $\mathcal{R}(x)$. Moreover, the special cases of a hard surface ($Z \to \infty$) and a pressure-release surface ($Z = 0$) give $\mathcal{R}(x) = \delta(x)$ and $\mathcal{R}(x) = -\delta(x)$ respectively, so that the standard solution using the method of images is recovered in these two cases. This convolution may therefore be seen as a generalization of the method of images to impedance surfaces (similar to, although different from, the complex line source generalization of the method of images in 3D [10]). This is further investigated in §6.

2.2. Inversion of the Fourier integral for the direct wave

We now manipulate and solve Eq. (9a) for $\hat{p}_{\text{dir}}$ explicitly. While this result is not new, it is presented here since the same technique will be used in §2.3 to obtain $\hat{p}_{\text{refl}}$, and the technique is easier to follow in the case of $\hat{p}_{\text{dir}}$. We first deform the contour of integration in Eq. (9a) onto the steepest descent contour. The details of this are given in AppendixA. The steepest descent contour, parameterized by $q \in \mathbb{R}$, is found (A.5) to be

given by

$$k_{\mathrm{sd}}(q) = \frac{\omega}{\beta^2}\left(\frac{x}{r} - M\right) - \frac{\mathrm{i}xq^2}{2r^2} + \frac{|y-y_s|q}{r^2}\sqrt{\mathrm{i}\omega r + \beta^2 q^2/4}, \tag{13a}$$

$$\alpha_{\mathrm{sd}}(q) = \frac{\omega|y-y_s|}{r} - \frac{\mathrm{i}\beta^2|y-y_s|q^2}{2r^2} - \frac{xq}{r^2}\sqrt{\mathrm{i}\omega r + \beta^2 q^2/4}, \tag{13b}$$

where $\beta^2 = 1 - M^2$, $r^2 = x^2 + \beta^2|y-y_s|^2$, and the branch $\mathrm{Re}\big(\sqrt{\mathrm{i}\omega r + \beta^2 q^2/4}\big) > 0$ is chosen so that the contour is traversed in the correct direction. An example of this contour is given later in Fig. 6. As shown in AppendixA, deforming the contour of integration in Eq. (9a) onto this steepest descent contour is possible, and no poles cross the contour in this process, so that

$$\hat{p}_{\mathrm{dir}}(x,y,t;y_s) = \frac{\mathrm{i}\mathrm{e}^{\mathrm{i}\omega t - \mathrm{i}\omega r(1-Mx/r)/\beta^2}}{4\pi}\int_{-\infty}^{\infty}\frac{\omega - Mk_{\mathrm{sd}}(q)}{\sqrt{\mathrm{i}\omega r + \beta^2 q^2/4}}\mathrm{e}^{-q^2/2}\,\mathrm{d}q. \tag{14}$$

While this is easily numerically tractable due to the $\mathrm{e}^{-q^2/2}$ term, in fact an exact solution is possible by making the substitution

$$-q^2/2 = (\mathrm{i} + \sinh\phi)\omega r/\beta^2, \qquad\qquad q\sqrt{\mathrm{i}\omega r + \beta^2 q^2/4} = -\cosh(\phi)\omega r/\beta, \tag{15}$$

yielding

$$\begin{aligned}\hat{p}_{\mathrm{dir}}(x,y,t;y_s) &= \frac{-\mathrm{i}}{4\beta}\left(\frac{\partial}{\partial t} + M\frac{\partial}{\partial x}\right)\Bigg[\mathrm{e}^{\mathrm{i}\omega\left(t+Mx/\beta^2\right)}\underbrace{\left(\frac{-1}{\mathrm{i}\pi}\right)\int_{-\infty}^{\infty-\mathrm{i}\pi}\exp\left\{\frac{\omega r}{\beta^2}\sinh\phi\right\}\mathrm{d}\phi}_{H_0^{(2)}\left(\omega r/\beta^2\right)}\Bigg] \\ &= \frac{\omega}{4\beta^3}\exp\left\{\mathrm{i}\omega\left(t + Mx/\beta^2\right)\right\}\left[H_0^{(2)}\left(\omega r/\beta^2\right) + \frac{\mathrm{i}Mx}{r}H_1^{(2)}\left(\omega r/\beta^2\right)\right],\end{aligned} \tag{16}$$

where the integral form of the Hankel function $H_0^{(2)}$ has been used [39, p. 360] and $H_0^{(2)\prime} = -H_1^{(2)}$. This is the convective derivative of the convected form of the classical outgoing cylindrical wave, as might have been expected for a line mass source in uniform flow; the presence of the convective derivative is due to the mass source on the right-hand-side of Eq. (1) containing a convective derivative of a delta function.

The form of Eq. (14) is easily amenable to far-field asymptotic analysis. As shown in AppendixA.2, Eq. (14) for $r \gg 1$ gives

$$\hat{p}_{\mathrm{dir}}(x,y,t;y_s) = \sqrt{\frac{\omega}{8\pi r}}\frac{1-Mx/r}{\beta^2}\exp\left\{\mathrm{i}\omega t - \mathrm{i}\omega r\frac{1-Mx/r}{\beta^2} + \mathrm{i}\pi/4\right\} + O\left(\frac{1}{\sqrt{\omega r^3}}\right). \tag{17}$$

This may also be verified by substituting the asymptotic expansion for large argument of $H_0^{(2)}$ and its derivative [39, pp. 364–365] into Eq. (16). Eq. (17) shows that the direct wave $\hat{p}_{\mathrm{dir}}$ consists of an outgoing cylindrical wave $r^{-1/2}\exp\{\mathrm{i}\omega(t-r)\}$ from the point $(0, y_s)$ modified by a Doppler factor of $(1 - Mx/r)/\beta^2$.

2.3. Inversion of the Fourier integral for the reflected wave

We will now apply the same procedure as in the previous section to $\hat{p}_{\mathrm{refl}}$, given by Eq. (9b). From AppendixA, the steepest descent contour in this case is given by

$$\hat{r}^2 = x^2 + \beta^2(y+y_s)^2, \tag{18a}$$

$$\hat{k}_{\mathrm{sd}}(q) = \frac{\omega}{\beta^2}\left(\frac{x}{\hat{r}} - M\right) - \frac{\mathrm{i}xq^2}{2\hat{r}^2} + \frac{|y+y_s|q}{\hat{r}^2}\sqrt{\mathrm{i}\omega\hat{r} + \beta^2 q^2/4}, \tag{18b}$$

$$\hat{\alpha}_{\mathrm{sd}}(q) = \frac{1}{\hat{r}^2}\left[\omega\hat{r}|y+y_s| - \mathrm{i}\beta^2|y+y_s|q^2/2 - xq\sqrt{\mathrm{i}\omega\hat{r} + \beta^2 q^2/4}\right]. \tag{18c}$$

However, unlike for the direct wave $\hat{p}_{\mathrm{dir}}$, we must now take care to deform onto the steepest descent contour without crossing any poles of the integrand, which are given in Eq. (10) by $D(k,\omega)=0$. As shown in AppendixA, deforming the contour of integration in Eq. (9b) onto this steepest descent contour is possible, giving

$$\begin{aligned}\hat{p}_{\mathrm{refl}}(x,y,t;y_s) = \frac{\mathrm{i}\mathrm{e}^{\mathrm{i}\omega t-\mathrm{i}\omega\hat{r}(1-Mx/\hat{r})/\beta^2}}{4\pi}\int_{-\infty}^{\infty}\frac{\hat{\alpha}_{\mathrm{sd}}(q)\omega Z-\left(\omega-M\hat{k}_{\mathrm{sd}}(q)\right)^2}{\hat{\alpha}_{\mathrm{sd}}(q)\omega Z+\left(\omega-M\hat{k}_{\mathrm{sd}}(q)\right)^2}\frac{\omega-M\hat{k}_{\mathrm{sd}}(q)}{\sqrt{\mathrm{i}\omega\hat{r}+\beta^2q^2/4}}\mathrm{e}^{-q^2/2}\,\mathrm{d}q\\ +\sum_{k\in\mathcal{K}_+}A_k\mathrm{e}^{\mathrm{i}\omega t-\mathrm{i}kx-\mathrm{i}\alpha|y+y_s|}-\sum_{k\in\mathcal{K}_-}A_k\mathrm{e}^{\mathrm{i}\omega t-\mathrm{i}kx-\mathrm{i}\alpha|y+y_s|}-A_{k_{\mathrm{HI}}}\mathrm{e}^{\mathrm{i}\omega t-\mathrm{i}k_{\mathrm{HI}}x-\mathrm{i}\alpha|y+y_s|},\end{aligned} \tag{19}$$

where $\mathcal{K}_+$ and $\mathcal{K}_-$ are the zeros of the dispersion relation $D=0$ lying either in the upper-half k-plane below the steepest descent contour ($\mathcal{K}_+$) or in the lower-half k-plane above the steepest descent contour ($\mathcal{K}_-$), k_{HI} is a zero of the dispersion relation $D=0$ representing a possible hydrodynamic instability discussed below, and

$$A_k=\frac{\mathrm{i}(\omega-Mk)^3}{\omega Z\big(\beta^2k+M\omega\big)+2M(\omega-Mk)\alpha-\alpha^2\omega\partial Z/\partial k}. \tag{20}$$

Note that $\mathcal{K}_+$ and $\mathcal{K}_-$ typically contain a small finite number of values of k (with a maximum of four values for a locally-reacting impedance) and may be empty. We therefore see that the poles of the integrand represent the triggering of surface waves, analogous to previous 2D and 3D results without flow [6, 7, 14]. The classification of the surface waves in Eq. (19) into $\mathcal{K}_+$ and $\mathcal{K}_-$ assumes that all surface waves are stable. However, for a locally reacting impedance Rienstra [4] suggested that one of the surface waves (denoted here by k_{HI}) might represent a hydrodynamic instability. Since k_{HI} is already classified into $\mathcal{K}_+$ and $\mathcal{K}_-$ as if it were stable, correcting this to consider k_{HI} as an instability is achieved by including the term explicitly involving k_{HI} in Eq. (19). Excluding this term (or equivalently setting $A_{k_{\mathrm{HI}}}=0$) yields the stable solution. The surface waves are discussed further in §5.

Unlike for $\hat{p}_{\mathrm{dir}}$, in general Eq. (19) is the best that can be done analytically for $\hat{p}_{\mathrm{refl}}$, and solution of Eq. (19) must proceed by numerical quadrature. However, due to the use of a steepest descent contour, the integral in Eq. (19) is both nicely decaying as $|q|\to\infty$ as $\mathrm{e}^{-q^2/2}$ and has no rapid oscillations as the exponent is entirely real; computation of this integral is therefore easily numerically tractable. Solution of the dispersion relation $D(k,\omega)=0$ is also readily tractable, especially in the locally reacting case when $Z(\omega)$ is independent of k for which $D(k,\omega)=0$ reduces to a quartic equation in k. Code to evaluate Eq. (19) is provided in the supplementary material, some example results of which are given in §4.

However, further progress may be made in the far field $\hat{r}\gg1$, for which Eq. (19) is readily amenable to asymptotic analysis. As shown in AppendixA.2, for $\hat{r}\gg1$, Eq. (19) gives

$$\begin{aligned}\hat{p}_{\mathrm{refl}} = \sqrt{\frac{\omega}{8\pi\hat{r}}}\frac{1-Mx/\hat{r}}{\beta^2}\left[\frac{Z(\hat{k}_s)\beta^4(y+y_s)/\hat{r}-(1-Mx/\hat{r})^2}{Z(\hat{k}_s)\beta^4(y+y_s)/\hat{r}+(1-Mx/\hat{r})^2}\right]\exp\left\{\mathrm{i}\omega t-\mathrm{i}\omega\hat{r}\frac{1-Mx/\hat{r}}{\beta^2}+\mathrm{i}\pi/4\right\}\\ +\sum_{k\in\mathcal{K}_+}A_k\mathrm{e}^{\mathrm{i}\omega t-\mathrm{i}kx-\mathrm{i}\alpha|y+y_s|}-\sum_{k\in\mathcal{K}_-}A_k\mathrm{e}^{\mathrm{i}\omega t-\mathrm{i}kx-\mathrm{i}\alpha|y+y_s|}-A_{k_{\mathrm{HI}}}\mathrm{e}^{\mathrm{i}\omega t-\mathrm{i}k_{\mathrm{HI}}x-\mathrm{i}\alpha|y+y_s|}+O\left(\frac{1}{\sqrt{\omega r^3}}\right),\end{aligned} \tag{21}$$

where $\hat{k}_s=\hat{k}_{\mathrm{sd}}(0)=(x/\hat{r}-M)\omega/\beta^2$. The supplementary material also provides code to evaluate Eq. (21).

Comparing Eq. (21) with Eq. (17) shows that $\hat{p}_{\mathrm{refl}}$ consists of an outgoing cylindrical wave from the point $(0,-y_s)$ with the same Doppler factors as $\hat{p}_{\mathrm{dir}}$ but with a directivity given by the term in square brackets in Eq. (21), together with a sum of surface waves.

2.4. Far-field directivity

We now consider the sound radiated to the far field. We take $x=R\sin\theta$ and $y=R\cos\theta$ so that downstream of the line source corresponds to $\theta>0$. We first note that

$$\sqrt{x^2+\beta^2(y-y_s)^2}=R\sqrt{1-M^2\cos^2\theta}-\frac{\beta^2y_s\cos\theta}{\sqrt{1-M^2\cos^2\theta}}+O\left(\frac{1}{R}\right). \tag{22}$$

Hence, using Eq. (17) and Eq. (21), $\hat{p} = \hat{p}_{\mathrm{dir}} + \hat{p}_{\mathrm{refl}}$ is given to leading order by

$$\hat{p} = \sqrt{\frac{\omega}{2\pi R}}\mathcal{D}(R,\theta)\mathrm{e}^{\mathrm{i}\phi(R,\theta)} \tag{23a}$$

where the phase ϕ and directivity $\mathcal{D}$ are given by

$$\phi(R,\theta) = \omega t - \frac{\omega R}{\beta^2}\Big(\sqrt{1-M^2\cos^2\theta} - M\sin\theta\Big) + \frac{\pi}{4}, \tag{23b}$$

$$\mathcal{D}(R,\theta) = \frac{\sqrt{1-M^2\cos^2\theta} - M\sin\theta}{\beta^2\big(1-M^2\cos^2\theta\big)^{3/4}}\hat{\mathcal{D}}\bigg(\frac{\sin\theta}{\sqrt{1-M^2\cos^2\theta}}, \frac{\cos\theta}{\sqrt{1-M^2\cos^2\theta}}\bigg), \tag{23c}$$

$$\text{where} \qquad \hat{\mathcal{D}}(X,Y) = \frac{\beta^4 Z_s Y\cos(\omega y_s Y) + \mathrm{i}(1-MX)^2\sin(\omega y_s Y)}{\beta^4 Z_s Y + (1-MX)^2}, \tag{23d}$$

and $Z_s = Z\big((X-M)\omega/\beta^2, \omega\big)$. It should be noted that, in deriving this far-field directivity, we have neglected the sum of surface waves in $\hat{p}_{\mathrm{refl}}$. This is justified for stable surface waves since such surface waves are exponentially decaying in $|x|$ and therefore are exponentially small compared with the far-field solution (23). If a hydrodynamic instability is present, this will be exponentially larger than the far-field solution (23) at angles for which it is excited, and it is not helpful to plot such exponentially large solutions when considering the far-field directivity. This can be seen in plots of the directivity given in Fig. 3 and Fig. 5, which are discussed in §4.

2.5. Overall solution

The overall solution for a line source over an impedance wall is given by $\hat{p}(x,y,y;y_s) = \hat{p}_{\mathrm{dir}}(x,y,t;y_s) + \hat{p}_{\mathrm{refl}}(x,y,t;y_s)$, where $\hat{p}_{\mathrm{dir}}$ is the direct field due to a line source in free space (i.e. with no impedance surface present) given explicitly in terms of Hankel functions in Eq. (16), and $\hat{p}_{\mathrm{refl}}$ is the field due to the reflection of the line source by the impedance surface given as a steepest-descent integral suitable for numerical computation in Eq. (19). Code to evaluate $\hat{p}$ using Eq. (16) and Eq. (19) is provided in the supplementary material. Eq. (19) shows that the line source also excites surface waves along the impedance surface given [as predicted by 4] by Eq. (10) for $D(k,\omega) = 0$, which are further investigated in §5. Since one of these surface waves might represent a hydrodynamic instability, but since the Myers [38] impedance boundary condition is unsuitable for this purpose [40], we next use the general analysis described already to introduce a modified impedance boundary condition.

3. Incorporating a modified impedance boundary condition

In this section, we utilize the flexibility afforded by having kept $Z(k,\omega)$ as a function of both k and ω to substitute for the Myers boundary condition (5) a modified boundary condition [31] to account for a thin boundary layer over the impedance surface. Here, we assume a constant-density linear boundary layer of thickness δ given by

$$U(y) = \begin{cases} M & y > \delta \\ My/\delta & y < \delta \end{cases}. \tag{24}$$

The impedance $Z(k,\omega)$ used in Eq. (5) is then replaced by an effective impedance $Z_{\mathrm{mod}}(k,\omega)$ that accounts for the effects of this boundary layer, given by

$$\mathrm{i}\omega Z_{\mathrm{mod}} = \frac{\mathrm{i}\omega Z - Mk\omega\delta + 2k^2M^2\delta/3}{1 + \mathrm{i}ZM\delta k^3(\omega - Mk)^{-2}}, \tag{25}$$

where the $Z(k,\omega)$ in Eq. (25) is the actual impedance of the surface. Note that the effective impedance Z_{mod} seen by the acoustic waves is nonlocally reacting (since it depends on both k and ω) even if the actual impedance of the surface Z were locally reacting and therefore independent of k. In making this change, only

the integrand of $\hat{p}_{\mathrm{refl}}$ and the amplitudes and wavenumbers of the surface waves A_k are changed. Eq. (19) then gives $\hat{p}_{\mathrm{refl}}(x, y, t; y_s)$ as

$$\begin{aligned}\hat{p}_{\mathrm{refl}} =& \frac{\mathrm{i}\mathrm{e}^{\mathrm{i}\omega t - \mathrm{i}\omega\hat{r}(1-Mx/\hat{r})/\beta^2}}{4\pi}\int_{-\infty}^{\infty}\frac{\omega - M\hat{k}_{\mathrm{sd}}}{\sqrt{\mathrm{i}\omega\hat{r} + \beta^2 q^2/4}}\mathrm{e}^{-q^2/2} \\ &\times \frac{\big(\omega Z + \mathrm{i}M\hat{k}_{\mathrm{sd}}\omega\delta - 2\mathrm{i}\hat{k}_{\mathrm{sd}}^2 M^2\delta/3\big)\hat{\alpha}_{\mathrm{sd}} - \big(\omega - M\hat{k}_{\mathrm{sd}}\big)^2 - \mathrm{i}MZ\delta\hat{k}_{\mathrm{sd}}^3}{\big(\omega Z + \mathrm{i}M\hat{k}_{\mathrm{sd}}\omega\delta - 2\mathrm{i}\hat{k}_{\mathrm{sd}}^2 M^2\delta/3\big)\hat{\alpha}_{\mathrm{sd}} + \big(\omega - M\hat{k}_{\mathrm{sd}}\big)^2 + \mathrm{i}MZ\delta\hat{k}_{\mathrm{sd}}^3}\,\mathrm{d}q \\ &+ \sum_{k\in\mathcal{K}_+^{\mathrm{mod}}} A_k^{\mathrm{mod}}\mathrm{e}^{\mathrm{i}\omega t - \mathrm{i}kx - \mathrm{i}\alpha|y+y_s|} - \sum_{k\in\mathcal{K}_-^{\mathrm{mod}}} A_k^{\mathrm{mod}}\mathrm{e}^{\mathrm{i}\omega t - \mathrm{i}kx - \mathrm{i}\alpha|y+y_s|} - A_{k_{\mathrm{HI}}}^{\mathrm{mod}}\mathrm{e}^{\mathrm{i}\omega t - \mathrm{i}k_{\mathrm{HI}}x - \mathrm{i}\alpha|y+y_s|},\end{aligned} \tag{26}$$

where $\hat{k}_{\mathrm{sd}}(q)$ and $\hat{\alpha}_{\mathrm{sd}}(q)$ are as in Eq. (18) and k_{HI}, $\mathcal{K}_+^{\mathrm{mod}}$ and $\mathcal{K}_-^{\mathrm{mod}}$ are defined as before but for solutions to the dispersion relation $D^{\mathrm{mod}}(k,\omega) = 0$, where

$$D^{\mathrm{mod}}(k,\omega) = \big(\omega Z + \mathrm{i}Mk\omega\delta - 2\mathrm{i}k^2M^2\delta/3\big)\alpha + \big(\omega - Mk\big)^2 + \mathrm{i}MZ\delta k^3 \tag{27}$$

is the surface wave dispersion relation of [15] although with a different branch cut taken for α, and A_k^{mod} are the respective surface wave amplitudes given by

$$A_k^{\mathrm{mod}} = \mathrm{i}(\omega - Mk)\frac{(\omega - Mk)^2 + \mathrm{i}MZ\delta k^3}{-\alpha\partial D/\partial k} \tag{28}$$

where

$$\begin{aligned}-\alpha\partial D/\partial k =& (\beta^2 k + M\omega)(\omega Z + \mathrm{i}Mk\omega\delta - 2\mathrm{i}k^2M^2\delta/3) - \mathrm{i}\alpha^2(M\omega\delta - 4kM^2\delta/3) \\ &+ 2M(\omega - Mk)\alpha - \alpha^2\omega\partial Z/\partial k - 3\mathrm{i}MZ\delta k^2\alpha - \mathrm{i}M\delta k^3\alpha\partial Z/\partial k.\end{aligned} \tag{29}$$

Eq. (26) may be easily computed using quadrature, as before, and code to do so is provided in the supplementary material. Moreover, the far-field asymptotics in AppendixA.2 give, for $\hat{r} \gg 1$,

$$\begin{aligned}\hat{p}_{\mathrm{refl}} =& \sqrt{\frac{\omega}{8\pi\hat{r}}}\frac{1 - Mx/\hat{r}}{\beta^2}\exp\left\{\mathrm{i}\omega t - \mathrm{i}\omega\hat{r}\frac{1 - Mx/\hat{r}}{\beta^2} + \mathrm{i}\pi/4\right\} \\ &\times\left[\frac{\big(Z + \mathrm{i}M\hat{k}_s\delta - 2\mathrm{i}\hat{k}_s^2M^2\delta/(3\omega)\big)(y+y_s)/\hat{r} - (1 - Mx/\hat{r})^2/\beta^4 - \mathrm{i}ZM\delta\hat{k}_s^3\omega^2}{\big(Z + \mathrm{i}M\hat{k}_s\delta - 2\mathrm{i}\hat{k}_s^2M^2\delta/(3\omega)\big)(y+y_s)/\hat{r} + (1 - Mx/\hat{r})^2/\beta^4 + \mathrm{i}ZM\delta\hat{k}_s^3\omega^2}\right] \\ &+ \sum_{k\in\mathcal{K}_+} A_k^{\mathrm{mod}}\mathrm{e}^{\mathrm{i}\omega t - \mathrm{i}kx - \mathrm{i}\alpha|y+y_s|} - \sum_{k\in\mathcal{K}_-} A_k^{\mathrm{mod}}\mathrm{e}^{\mathrm{i}\omega t - \mathrm{i}kx - \mathrm{i}\alpha|y+y_s|} - A_{k_{\mathrm{HI}}}^{\mathrm{mod}}\mathrm{e}^{\mathrm{i}\omega t - \mathrm{i}k_{\mathrm{HI}}x - \mathrm{i}\alpha|y+y_s|} + O\left(\frac{1}{\sqrt{\omega r^3}}\right),\end{aligned} \tag{30}$$

where, as before, $\hat{k}_s = (x/\hat{r} - M)\omega/\beta^2$. The modified impedance boundary condition has therefore modified the directivity of the outgoing cylindrical wave (given by the term in square brackets), and has also modified the number and nature of the surface waves [as described by 15].

4. Numerical results

To illustrate the above results, we here give numerical examples; the code used to produce these results is available in the supplementary material. Table 1 describes the two cases presented: case 1 uses the Myers boundary condition, with parameters intended to be typical of aeroacoustics, while case 2 demonstrates the use of the modified impedance boundary condition, as derived in §3.

4.1. Numerical results for the Myers boundary condition

Fig. 2 plots a snapshot of the pressure $\hat{p}$ in the x-y plane for case 1, computed using Eq. (16) and Eq. (19). Fig. 2(a) shows the impedance surface absorbing sound in the downstream direction, as demonstrated by

	ω	M	δ	y_s	$Z(\omega)$	k_{HI}
case 1	31	0.5	0	0.3	$0.75 + 0.01\mathrm{i}\omega - 10\mathrm{i}/\omega$	$\approx 112 + 105\mathrm{i}$
case 2	50	0.4	10^{-2}	0.3	$2 + 0.03\mathrm{i}\omega - 60\mathrm{i}/\omega$	$\approx 113 + 5\mathrm{i}$

Table 1: Table of parameters used for the two cases evaluated numerically here. A value of $\delta = 0$ indicates evaluation using the Myers, rather than the modified, boundary condition.

(a) stable

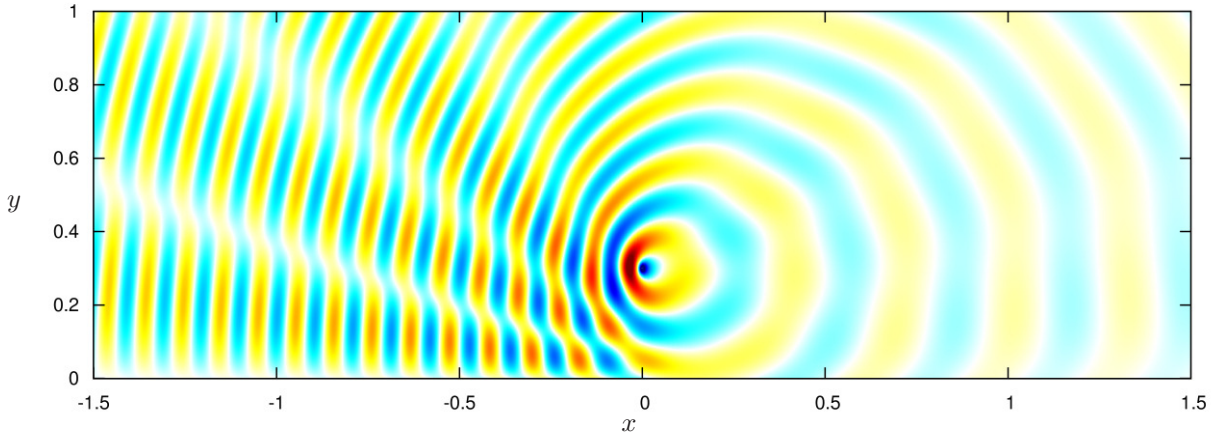

(b) unstable

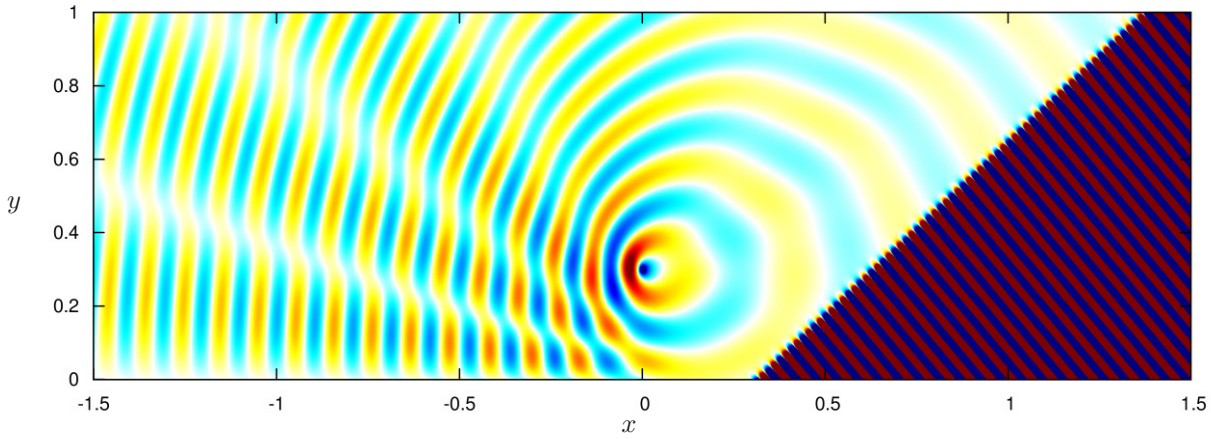

Figure 2: Snapshot of the pressure field ($\mathrm{Im}(\hat{p})$) in the x-y plane for case 1, calculated using Eq. (16) and Eq. (19). Parameters are given in table 1. (a) assumes all surface waves are stable, while (b) assumes the k_{HI} surface wave to be an instability.

the lack of an interference pattern in this region, although some beaming at three oblique upstream angles and a fourth weaker beam at an angle nearly normal to the surface is present. Fig. 2(b) shows the result if the k_{HI} surface wave is assumed to be an instability, and clearly shows the surface wave being launched from the image point $y = -y_s$ at a well-defined angle. Note that, apart from the presence of this instability, Fig. 2(a) and Fig. 2(b) are almost identical.

Fig. 3 plots the far-field directivity for case 1 computed using the far-field asymptotics (23) together with the actual solution computed using Eq. (16) and Eq. (19) at a large distance $R = 50$ and a small distance $R = 2$ from the origin. As expected, the analytic and asymptotic results are indistinguishable for $R = 50$, and although the match at $R = 2$ is not perfect, it is still surprisingly good. The three strong upstream beaming directions and the fourth weaker nearly-normal beaming direction are clearly visible, as is the fact

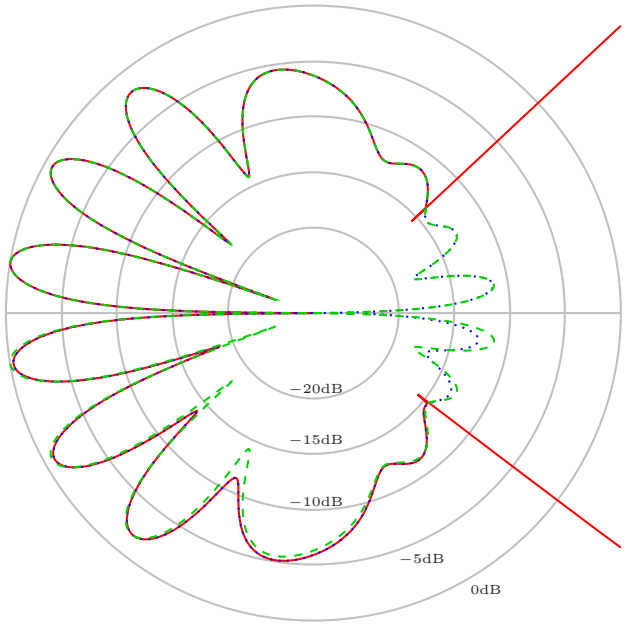

Figure 3: The far-field directivity (in terms of sound pressure level on a decibel scale) for case 1. Parameters are given in table 1. (top) at a distance $R = 50$ from the origin. (bottom) at a distance $R = 2$ from the origin. Solid line: analytic solution (16, 19) with k_{HI} assumed unstable. Dotted line: analytic solution (16, 19) with all surface waves assumed stable. Dashed line: far-field asymptotics given by Eq. (23).

that far more sound is radiated upstream than downstream, in agreement with Fig. 2(a). Also in agreement with Fig. 2(b), the effect of treating the k_{HI} surface wave as an instability is to dominate the directivity for a range of observation angles downstream of the line source, but to otherwise leave the far-field directivity almost unaltered.

4.2. Numerical results for the modified boundary condition

Fig. 4 plots the r.m.s. time-average of the pressure $\hat{p}$ in the x-y plane for case 2, computed using Eq. (16) and Eq. (26). For these parameters, Fig. 4(a) shows beaming both upstream and downstream of the source, although more sound is still radiated upstream than downstream. Fig. 4(b) shows the same result if the surface wave k_{HI} is considered to be an instability. The surface wave is again seen to be launched from the image point $y = -y_s$ at a well-defined angle, which for these parameters is a very shallow angle. Again, apart from the presence of this instability, Fig. 4(a) and Fig. 4(b) are almost identical.

Fig. 5 shows the corresponding far-field directivity for case 2, comparing the far-field directivity computed using Eq. (23) with Z replaced by Z_{mod} from Eq. (25), and the exact solution computed using Eq. (16) and Eq. (26) at a large distance $R = 50$ and a small distance $R = 2$ from the origin. The directivity pattern clearly matches with that shown in Fig. 4. Once again, the exact and asymptotic results are indistinguishable for $R = 50$ and show reasonable agreement at the much closer distance $R = 2$. Note that the instability is present at shallow downstream angles for $R = 50$, but has not yet grown sufficiently to be seen for $R = 2$, and that the directivity with k_{HI} assumed unstable is indistinguishable from the directivity with k_{HI} assumed stable everywhere outside the region that the instability dominates.

5. Surface waves

In the analysis of §2 and §3 above, the reflected wave $\hat{p}_{\mathrm{refl}}$ has consisted of a steepest-descent integral and a sum of surface waves. The surface waves are given by a dispersion relation $D(k, \omega) = 0$, with D being given by Eq. (10) for the Myers impedance boundary condition and Eq. (27) for the modified impedance boundary

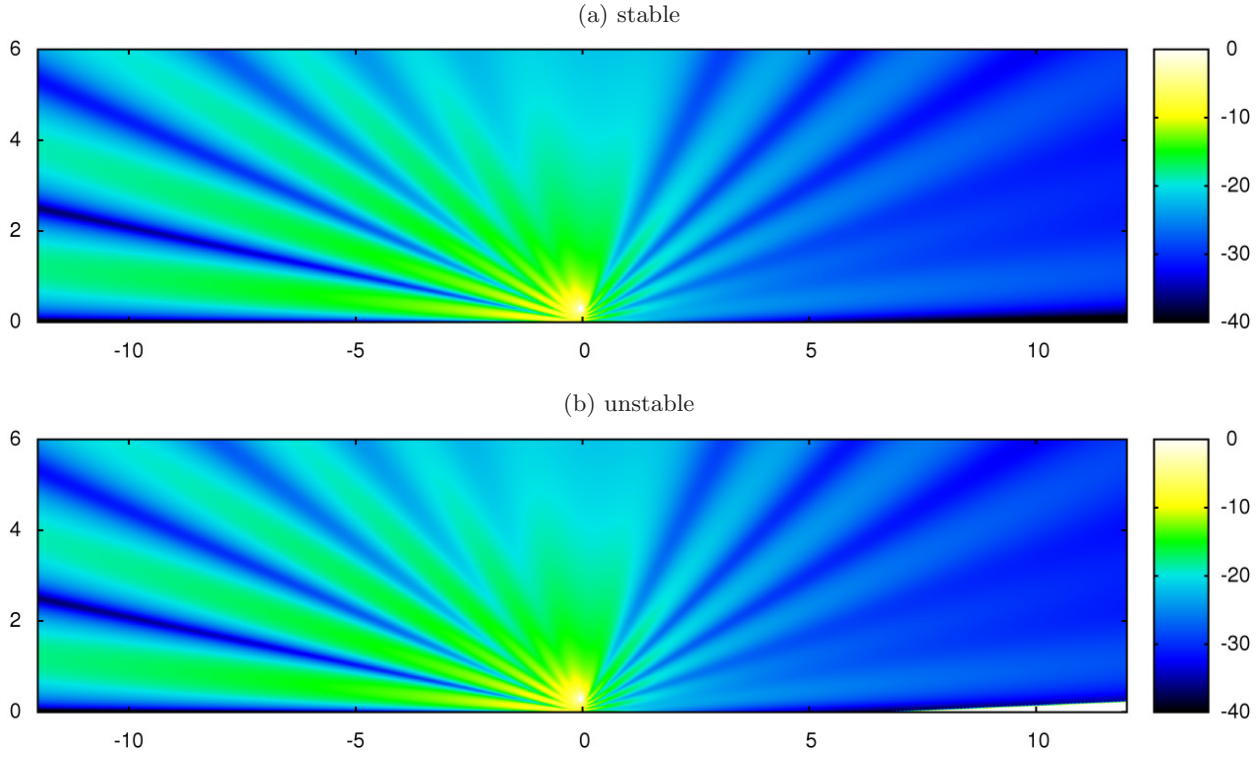

Figure 4: Time-averaged r.m.s. pressure amplitude ($|\hat{p}|/\sqrt{2}$) on a dB scale in the x-y plane for case 2, calculated using Eq. (16) and Eq. (26). Parameters are given in table 1. (a) assumes all surface waves are stable, while (b) assumes the k_{HI} surface wave to be an instability. (The instability is visible in the bottom right hand corner.)

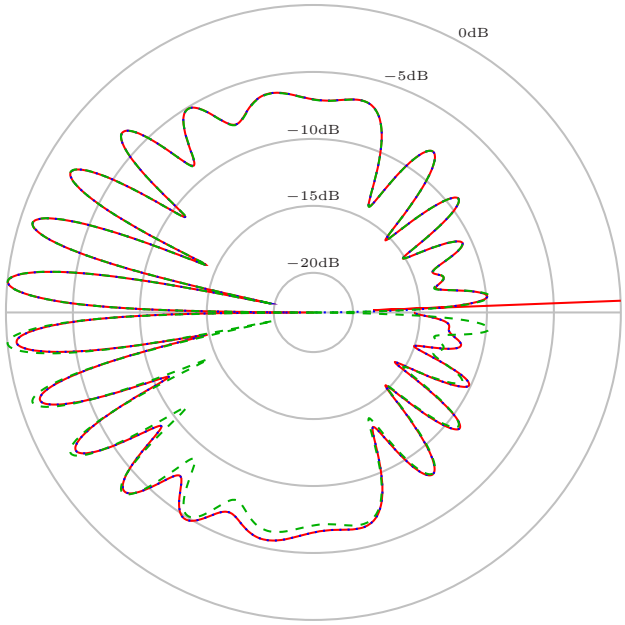

Figure 5: The far-field directivity (in terms of sound pressure level on a decibel scale) for case 2. Parameters are given in table 1. (top) at a distance $R = 50$ from the origin. (bottom) at a distance $R = 2$ from the origin. Solid line: analytic solution (16, 26) with k_{HI} assumed unstable. Dotted line: analytic solution (16, 26) with all surface waves assumed stable. Dashed line: far-field asymptotics given by Eq. (23) with Z replaced by Z_{mod} from Eq. (25).

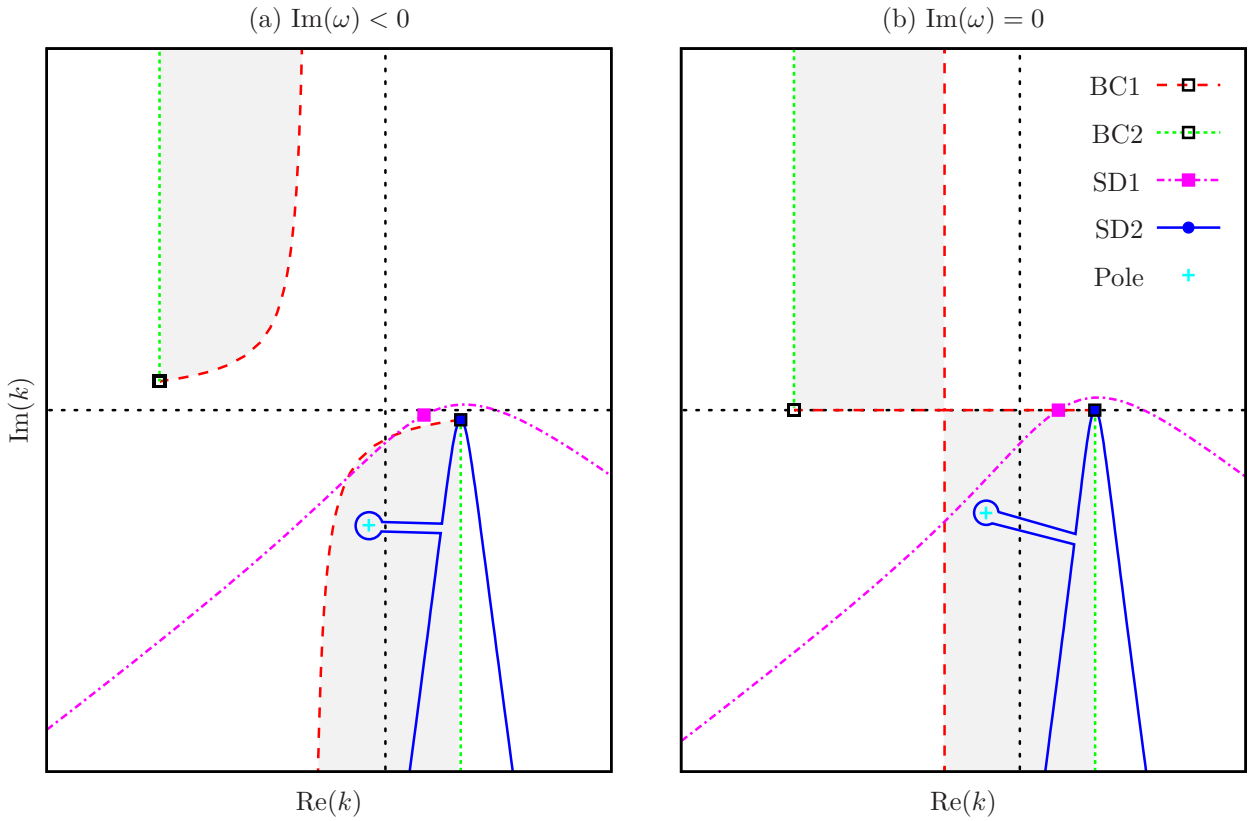

Figure 6: Sketch in the k-plane of the possible choices for the branch cuts of $\alpha(k)$ and the steepest descent contours for $\hat{p}_{\mathrm{dir}}(x, Y + y_s, t; y_s)$ and $\hat{p}_{\mathrm{refl}}(x, Y - y_s, t; y_s)$. BC1 is the branch cut for alpha given by requiring $\mathrm{Im}(\alpha(k)) < 0$. BC2 is the branch cut given by Eq. (32). The shaded region indicates where $\mathrm{Im}(\alpha(k)) > 0$ for branch cut BC2. SD1 is the steepest descent contour for $x/|Y| = 1$. SD2 is the steepest descent contour for $x/|Y| = 10$. Points on the steepest descent contours indicate the saddle point. Poles of the integrand of Eq. (9b) are also marked.

condition. For a locally reacting impedance, Eq. (10) is exactly the dispersion relation for surface waves found by Rienstra [4], which was shown to have up to four solutions, one of which might be a hydrodynamic instability. Eq. (27) is exactly the surface wave dispersion relation found by Brambley [15], which was shown for a locally reacting impedance to have at most six solutions, one of which is a hydrodynamic instability (for a discussion of stability, see Refs. 31, 40). However, both dispersion relations D involve the radial wavenumber α, and since $\alpha^2 = (\omega - Mk)^2 - k^2$ there are two possible choices for the sign of α. Both Rienstra [4] and Brambley [15] took $\mathrm{Im}(\alpha(k)) < 0$ for all k, justified by requiring exponential decay of the surface waves away from the surface since surface waves have the form $\hat{p}_{\mathrm{SM}} \propto \exp\{\mathrm{i}\omega t - \mathrm{i}kx - \mathrm{i}\alpha y\}$. We now investigate the surface waves that are excited by a line-source above the impedance surface while only making the correct and necessary assumption that $\mathrm{Im}(\alpha(k)) < 0$ for real k (implied by causality since we have taken $\mathrm{Im}(\omega) < 0$), which we will see fixes a different choice of α leading to surface waves that can grow exponentially with distance from the surface. The contour deformation of the Fourier inversion contour onto the steepest descent contour is only valid provided a continuous choice of $\alpha(k)$ is made along the contour. Since the choice of sign of α is equivalent to the choice of branch cut for $\sqrt{(\omega - Mk)^2 - k^2}$, this is equivalent to the statement that the the Fourier inversion contour should never cross the branch cut for this square root during the contour deformation process.

Fig. 6 shows the complex k-plane and two example steepest descent contours given by k_{sd} from Eq. (13) with $Y = |y - y_s|$ and $\hat{k}_{\mathrm{sd}}(q)$ from Eq. (18b) with $Y = y + y_s$. The shape of these contours is only a function of the angle of observation and not of the distance between source and observer. To see this, we set

$x = \hat{r}(x,y)\sin(\tilde{\theta})$ and $y + y_s = \hat{r}(x,y)\cos(\tilde{\theta})/\beta$, and reparameterize the steepest descent curve by $\hat{q} = \hat{r}^{-1/2}q$. Eq. (18b) then gives

$$\hat{k}_{\rm sd}(\hat{q}) = \frac{\omega}{\beta^2}\Big(\sin\tilde{\theta} - M\Big) - \mathrm{i}\sin(\tilde{\theta})\hat{q}^2/2 + |\cos(\tilde{\theta})|\hat{q}\sqrt{\mathrm{i}\omega + \beta^2\hat{q}^2/4}, \tag{31}$$

which can be seen to be independent of the observer distance $\hat{r}$. Since which surface waves are excited (by being included in $\mathcal{K}_\pm$) depends on which side of the poles the steepest descent contour runs, which surface waves are excited is therefore a function of the observer angle but not the distance from the source; i.e. particular surface waves get turned off or on[3] at particular observation angles. We may therefore modify the condition that surface waves decay as $y \to \infty$, as was argued by Rienstra [4] and Brambley [15] for the choice of branch cut of α, and instead specify that only surface waves which are excited for $\tilde{\theta} = 0$ (i.e. that are observed normal to the surface) need decay as $y \to \infty$.

However, Fig. 6 also shows that we are restricted in which branch cuts may be chosen for α, since the steepest descent contour is given and $\alpha(k)$ must be chosen to be a continuous branch along the contour (as indeed it is for $\alpha_{\rm sd}$ given by Eq. (13b)). The branch cut chosen by Rienstra [4] and Brambley [15] is shown as BC1 in Fig. 6, and can be seen to be crossed by the steepest descent contour for $x/|Y| = 10$. Considering $|Y| \to 0$ shows that there is only one possible branch cut for $\alpha(k)$ that is not crossed by any steepest descent contour, shown in Fig. 6 as BC2. That branch is given by

$$\alpha(k) = -\mathrm{i}\beta\,\mathrm{sqrt}\big(\mathrm{i}(k + \omega/(1-M))\big)\mathrm{sqrt}\big(-\mathrm{i}(k - \omega/(1+M))\big) \tag{32}$$

where $\mathrm{sqrt}(\eta) = \sqrt{\eta}$ with $\mathrm{Re}\big(\mathrm{sqrt}(\eta)\big) > 0$; conveniently, this is often the branch of the square root that is implemented by numerical libraries, such as FORTRAN's `SQRT` or C's `csqrt` functions. Note that this choice of branch means that $\mathrm{Im}(\alpha) > 0$ for some values of k (indicated by the shaded regions in Fig. 6). This implies that some surface waves that are excited in fact have $\mathrm{Im}(\alpha) > 0$ and so grow exponentially as $y \to \infty$. These are what were termed *fake surface waves* by Brambley and Peake [41]. Hence, "actual" surface waves with $\mathrm{Im}(\alpha) < 0$ in the shaded regions of Fig. 6 will not be excited by a line source over an impedance surface, while "fake" surface waves with $\mathrm{Im}(\alpha) > 0$ will be excited for certain radiation angles provided they lie within the shaded regions of Fig. 6; Fig. 6(b) shows a "fake" surface wave (denoted by $+$) that is present in $\mathcal{K}_-$ for $x/|Y| = 10$ but not for $x/|Y| = 1$. As an actual example, Fig. 7 shows the location of the surfaces waves in the k-plane for case 2. The surface waves that are excited for at least some angles by a line source above the impedance surface are shown as $+$, while the surface waves predicted by Brambley [15] are shown as $\times$. Two surface waves with $\mathrm{Im}(\alpha) < 0$ are never excited, while one surface wave with $\mathrm{Im}(\alpha) > 0$ is excited and is observed downstream of the line source at shallow angles to the impedance surface (i.e. $\tilde{\theta}$ close to $\pi/2$). The surface wave with $k \approx 113 + 5\mathrm{i}$ with $\mathrm{Im}(\alpha) < 0$ is excited by the line source for a certain range of observation angles, and indeed this surface waves is predicted by Brambley [15] to be a downstream-propagating instability $k_{\rm HI}$.

The fact that surface waves need not decay as $y \to \infty$ was noted by Crighton [18], who termed such waves "leaky waves", as sketched in Fig. 8. Crighton found that supersonic surface waves running along the surface (from A towards C in Fig. 8) launched oblique acoustic waves into the fluid (denoted by AD, BE and CF in Fig. 8). Since the supersonic surface wave is loosing energy to the fluid by radiating waves, it decays exponentially away from the source (decaying in x from the point A in Fig. 8). For a fixed x location (for example, the dashed vertical line in Fig. 8), as y is increased the observer is looking first at the wave CF launched from the surface at point C, and then at the wave BE launched from the surface at point B closer to the source, which is therefore exponentially larger in amplitude; hence, the disturbance in the fluid is expected to grow exponentially as the distance y from the surface increases. As y is increased further, there comes a point (or, rather, an observation angle, shown as θ in Fig. 8) for which the oblique wave AD launched at the source is seen, and for y larger than this no oblique waves generated from the surface exist. That is, there should be a cutoff observation angle, and indeed this is what we find here.

[3] More correctly, the surface waves turn off and on within a Fresnel region.

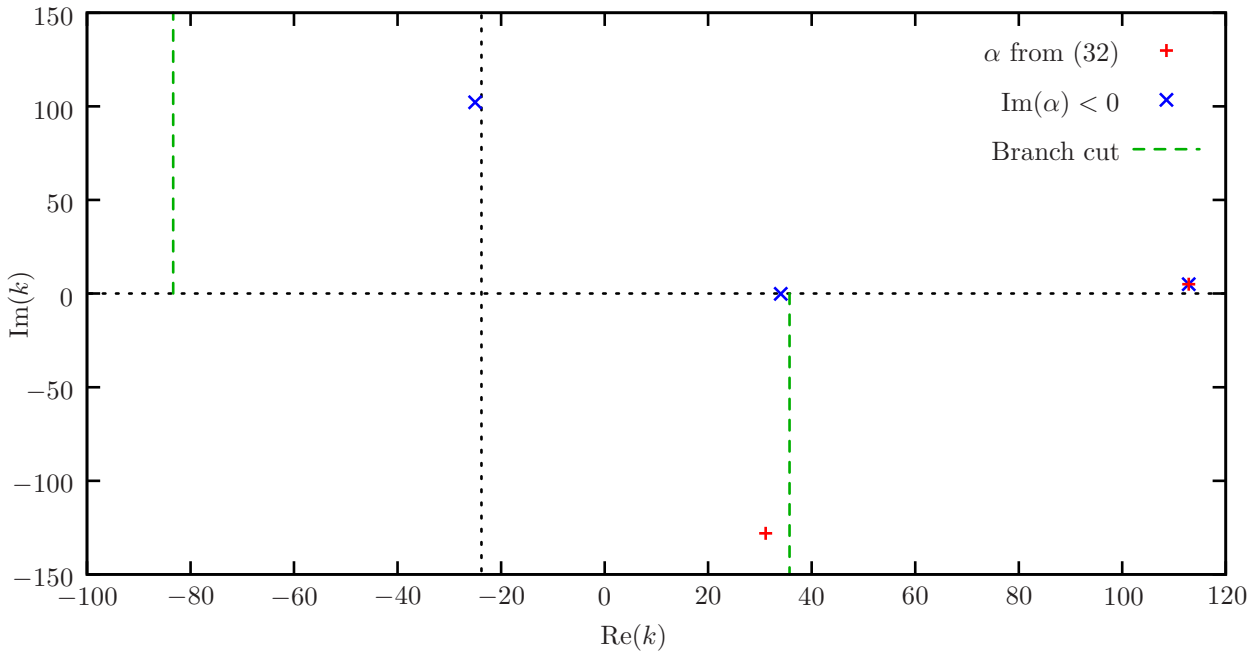

Figure 7: Surface waves for case 2. Plotted in the k-plane are surface waves with α as required for excitation by a line source (+, given by Eq. (32) and corresponding to branch cut BC2 in figure 6), and surface waves predicted by Brambley [15] given by the same Eq. (27) but with $\mathrm{Im}(\alpha) < 0$ (×, corresponding to branch cut BC1 in figure 6).

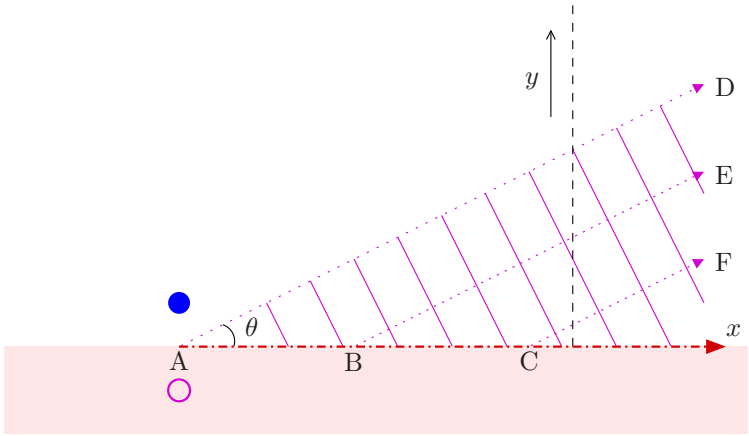

Figure 8: Schematic diagram of a line source (•) and its mirror image (○) generating a "leaky" supersonic surface wave (dashdot arrow) which launches an oblique wave into the fluid (wavevectors denoted by dotted lines, wave crests denoted by solid lines). The dashed line shows a path with x fixed and y increasing.

6. The generalized reflection coefficient at an impedance wall

We have seen in §2.3 that the reflected wave $\hat{p}_{\mathrm{refl}}$ can be seen in the far field $\hat{r} \gg 1$ as a Doppler shifted cylindrical wave with variable directivity together with a sum of surface waves. However, as mentioned in §2.1 and described schematically in Fig. 1, $\hat{p}_{\mathrm{refl}}$ can also be viewed as the result of a line of line sources along $y = -y_s$ with strengths given by a generalized reflection coefficient $\mathcal{R}(x)$ (11, 12). Here, we investigate the generalized reflection coefficient $\mathcal{R}(x)$ further, and show how this can be interpreted as a generalization of the classical method of images which is similar to, although different from, the complex line source generalization of the method of images for a point source in 3D described by, for example, Taraldsen [10].

Note that $\mathcal{R}(x)$ in Eq. (12) is independent of y_s, and that the convolution (11) is independent of Z, so that all the information about the impedance surface is contained within $\mathcal{R}(x)$. The special cases of a hard wall with $Z=\infty$ and a pressure-release surface with $Z=0$ result in $\mathcal{R}(x)=\delta(x)$ and $\mathcal{R}(x)=-\delta(x)$ respectively. However, in all but these two special cases, obtaining $\hat{p}_{\text{refl}}$ via a convolution over $\mathcal{R}(x)$, as given in Eq. (11), is not an effective numerical method for computing $\hat{p}_{\text{refl}}$; instead, the formula in Eq. (19) consisting of an easily tractable steepest-descent integral and a sum of surface waves is much faster and more robust. However, $\mathcal{R}(x)$ contains all information about the impedance surface, and may therefore give insight into the character of the reflected wave.

In what follows, we assume a locally reacting impedance; the corresponding derivation for certain non-locally reacting impedances is given in AppendixB. For a locally reacting impedance, meaning that $Z(\omega)$ is a function of ω only and is independent of k, the integrand of Eq. (12) is $O(1)$ as $k\to\pm\infty$, leading to a delta-function singularity in $\mathcal{R}(x)$. Multiplying out $\mathcal{R}(x)$ in this case gives

$$\mathcal{R}(x) = -\delta(x) + \underbrace{\frac{1}{2\pi}\int_{-\infty}^{\infty}\frac{2\alpha\omega Z}{\alpha\omega Z+(\omega-Mk)^2}\mathrm{e}^{-\mathrm{i}kx}\,\mathrm{d}k}_{I_0(x)} \tag{33a}$$

$$= -\delta(x) - \frac{\beta\omega Z}{M^2}\mathrm{e}^{\mathrm{i}\omega Mx/\beta^2}H_0^{(2)}\!\left(\frac{\omega|x|}{\beta^2}\right) + \underbrace{\frac{1}{2\pi}\int_{-\infty}^{\infty}\frac{2\omega^2 Z(\omega-2Mk+\beta^2\alpha Z)}{M^2\alpha\big[\alpha\omega Z+(\omega-Mk)^2\big]}\mathrm{e}^{-\mathrm{i}kx}\,\mathrm{d}k}_{I_1(x)}. \tag{33b}$$

Note that the integrand of I_0 in Eq. (33a) has no pole at $\alpha=0$, but is $O(1/|k|)$ as $|k|\to\infty$, leading to a logarithmic singularity of I_0 at $x=0$, while I_1 in Eq. (33b) is $O(1/|k|^2)$ as $|k|\to\infty$, so is expected to be regular at $x=0$, but introduces a pole at $\alpha=0$. Applying Jordan's lemma to I_0 gives

$$\mathcal{R}(x) = -\delta(x) + I_0^{\text{sd}}(x) \mp \sum_{k\in\mathcal{K}_\mp}\frac{2\alpha A_k}{\omega-Mk}\mathrm{e}^{-\mathrm{i}kx}, \tag{34}$$

where A_k is given by Eq. (20), $\pm$ is $+$ for $x>0$ and $-$ for $x<0$, and $\mathcal{K}_+$ and $\mathcal{K}_-$ are the zeros of the dispersion relation $D(k,\omega)=0$ given by Eq. (10) that should be considered to be above $(+)$ or below $(-)$ the inversion contour[4]. The integral $I_0^{\text{sd}}(x)$ is the contribution from deforming the integration contour of $I_0(x)$ onto the steepest descent contour (given by setting $Y=0$ in AppendixA), given by

$$I_0^{\text{sd}}(x) = \frac{\mathrm{i}\exp\big\{-\mathrm{i}\omega(\pm1-M)x/\beta^2\big\}}{\pi|x|}\int_{-\infty}^{\infty}\frac{q\mathrm{e}^{-q^2/2}\,\mathrm{d}q}{1+\dfrac{2|x|\omega}{Z\beta^5 q\sqrt{q^2+4\mathrm{i}\omega|x|/\beta^2}}\left(1\mp M\left(1-\dfrac{\mathrm{i}q^2\beta^2}{2\omega|x|}\right)\right)^2}, \tag{35}$$

where the branch of the square root is chosen such that $\sqrt{q^2+4\mathrm{i}\omega|x|/\beta^2}\sim q$ as $q\to+\infty$, with the branch cuts taken away from the real q axis.

We may write $I_0^{\text{sd}}(x) = -(\beta\omega Z/M^2)\mathrm{e}^{\mathrm{i}\omega Mx/\beta^2}H_0^{(2)}\big(\omega|x|/\beta^2\big) + I_1^{\text{sd}}(x)$, where $I_1^{\text{sd}}(x)$ is the steepest descent contour contribution from the I_1 integral, given by

$$I_1^{\text{sd}}(x) = \frac{Z\beta^2}{\pi M^2}\sqrt{\frac{\omega}{|x|\pi}}\mathrm{e}^{-\mathrm{i}\omega x(\pm1-M)/\beta^2+\mathrm{i}\pi/4}\int_{-\infty}^{\infty}\frac{(\pm1-M)^2\pm\frac{\mathrm{i}q^2\beta^2M}{\omega|x|}+\frac{\mathrm{i}\beta^4Zq}{\sqrt{\mathrm{i}\omega|x|}}\sqrt{1-\frac{\mathrm{i}q^2\beta^2}{4|x|\omega}}}{\left(1-\frac{\mathrm{i}q^2\beta^2}{4|x|\omega}\right)\left(\frac{\mathrm{i}Z\beta^4q}{\sqrt{\mathrm{i}\omega|x|}}+\frac{\left(\pm1-M+\frac{\mathrm{i}q^2\beta^2M}{2\omega|x|}\right)^2}{\sqrt{1-\frac{\mathrm{i}q^2\beta^2}{4\omega|x|}}}\right)}\mathrm{e}^{-q^2/2}\,\mathrm{d}q. \tag{36}$$

Note that Eq. (36) is regular at $q=0$, which corresponds to $\alpha=0$.

Fig. 9 plots $\mathcal{R}(x)$ for case 1. Plotted are the solutions calculated via Eq. (33a) and Eq. (33b), denoted

[4]If a pole in the upper-half k-plane is to be considered a hydrodynamic instability, then it should be considered to be below the contour and therefore be included in $\mathcal{K}_-$ rather than $\mathcal{K}_+$.

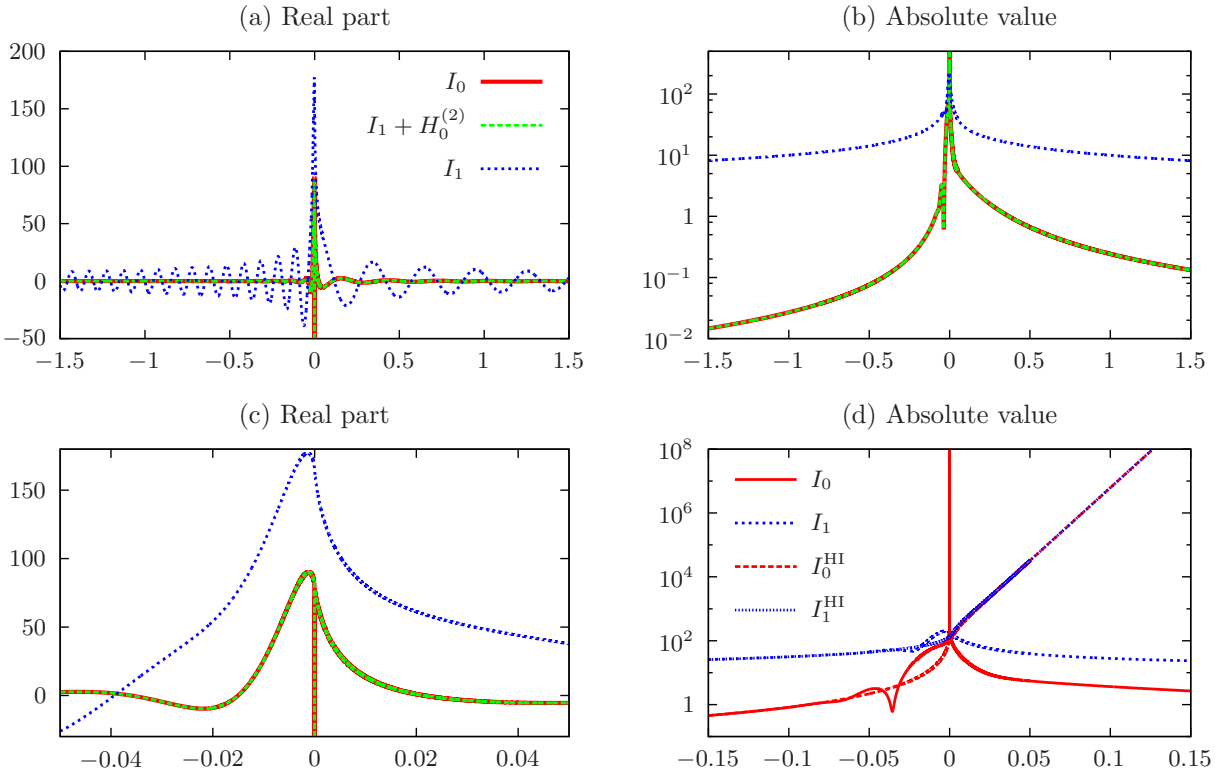

Figure 9: Plots of $\mathcal{R}(x)$ against x for case 1, evaluated using Eq. (33a) (labelled I_0) and Eq. (33b) (labelled $I_1 + H_0^{(2)}$), together with the I_1 integral from Eq. (33b) (labelled I_1). For I^{HI} only, the surface wave k_{HI} is assumed to be an instability.

as I_0 and $I_1 + H_0^{(2)}$ in Fig. 9, which are both expected to give the same answer $\mathcal{R}(x)$; also plotted is the I_1 integral on its own without the corresponding $H_0^{(2)}$ Hankel function. In all cases, the integrals are computed using I_0^{sd} and I_1^{sd} given by (34–36) using the code available in the supplementary material. Fig. 9(a) shows the real part, demonstrating oscillatory behaviour and rapid variation near $x = 0$. Fig. 9(c) zooms in near $x = 0$ and demonstrates the logarithmic singularity of $\mathcal{R}$ at $x = 0$, which comes from $I_0(x)$ in Eq. (33a) and from $H_0^{(2)}$ in Eq. (33b). The $I_1(x)$ integral can be seen to be regular at $x = 0$ in Fig. 9(c), as expected. Fig. 9(b) plots instead the absolute values $|\mathcal{R}(x)|$ and $|I_1(x)|$. This shows that while I_1 is indeed regular at $x = 0$, the pole of the integrand at $\alpha = 0$ gives a far slower decay as $|x| \to \infty$ compared with I_0. It is therefore likely that the most accurate computation of $\mathcal{R}(x)$ is given by Eq. (33b) for small $|x|$ and by Eq. (33a) for large $|x|$.

Fig. 9(d) shows the effect of treating the k_{HI} surface wave as a hydrodynamic instability. The exponential increase in $|I_0^{\mathrm{HI}}|$ and $|I_1^{\mathrm{HI}}|$ as $x \to \infty$ can clearly be seen, but note too the corresponding effect in I_0 and I_1 for $x < 0$ if that surface wave is instead included as a stable wave.

7. Conclusion

An exact analytic easily-computable solution (16, 19) has been presented for a time-periodic line mass source over a locally or nonlocally reacting impedance surface, together with closed-form expressions for the far-field sound radiated (23). Both may be computed using the computer code provided in the supplementary material. The solution may also be written using a generalized reflection coefficient as a convolution of a line of line sources (11), which is not useful for numerical evaluation but which demonstrates a generalization of the method of images for line sources above finite-impedance surfaces. This generalization is similar to the

3D point-source generalization, but involves a line of line sources running parallel to the surface, whereas for a 3D point source the generalization is of a line of point sources running perpendicular to the surface [5] or perpendicular to the surface with an imaginary normal coordinate [10]. While many previous studies have expressed the reflected wave as either a hard-wall or pressure-release solution plus a correction, §6 shows that for a locally reacting surface the natural expression is as a correction to a pressure-release solution, while AppendixB shows that for certain nonlocally reacting surfaces the natural expression is as a correction to a hard-wall solution.

The surface waves previously identified from poles of the integrand for a point or line source above an impedance surface without flow remain present with flow, and are here shown to correspond to the surface wave modes predicted for flow over an impedance surface [4, 15]. In the analysis presented here we have not attempted to ascertain the stability of these surface waves, but have instead allowed them to be treated as if they were stable or unstable. (For a proper stability analysis of the surface waves, see [15, 31].) It is interesting to note from the results presented in Fig. 2 and Fig. 4 that the hydrodynamic surface wave, if present, appears to originate from the image line source location $(x, y) = (0, -y_s)$. In cases where the stability of these surface waves is questionable, such as for a locally reacting impedance applied using the Myers boundary condition [40], this degree of flexibility would allow the stability of the surface waves to be inferred from experimental or numerical results. An important implication from this work is that the assumption by Rienstra [4] and Brambley [15] that surface waves necessarily decay away from the surface is not true, as was known by Crighton [18] for "leaky waves", and indeed we *we find here leaky surface waves excited by a line source that grow exponentially away from the surface.* This suggests that the thorough analysis of the number and nature of surface waves with flow previously performed may need to be modified.

Since the situation described here of a line source in uniform flow over an impedance surface in 2D is sufficiently simple to be quickly implementable in numerical 2D acoustics simulations, and since the exact analytic solution is available and computable using the computer code in the supplementary information, it is hoped that this test case might form a useful benchmark by which 2D numerical acoustic simulations may be quickly validated.

A number of extensions and generalizations of the work presented here are possible. For example, the 2D line source could be extended to a dipole or quadrupole line source, as was done for a 3D point dipole and quadrupole by Li, Taherzadeh, and Attenborough [42] and Li and Taherzadeh [43] respectively. The leading-order asymptotic far-field solutions (17, 21) given here could be extended to further orders, as was done for a 3D point source by Thomasson [8] and Rawlins [9], or extended to include the Fresnel regions where one of the surface wave poles nearly coincides with the steepest descent contour. The infinite extent of the impedance surface in the x-direction could be changed to a finite-width impedance section of an otherwise rigid surface, possibly using a Wiener–Hopf technique, as was done without a localized source for a mode in a waveguide in 2D by Koch [44] and in 3D by Rienstra [45]. Finally, the 3D point source solution could be investigated with mean flow included.

Acknowledgements

E.J. Brambley gratefully acknowledges the support of the Royal Society through a University Research Fellowship. A preliminary version of some parts of this paper was presented as part of AIAA Paper 2013-2218 at the 19th AIAA/CEAS Aeroacoustics Conference in Berlin, Germany [1].

AppendixA. Steepest descent derivation

In this appendix we derive the steepest descent contours for, and the far-field asymptotics of, integrals of the form

$$I(x,Y) = \int_{-\infty}^{\infty} f\left(\frac{k}{\omega}, \frac{\alpha}{\omega}\right) \frac{(\omega - Mk)}{4\pi\alpha} \mathrm{e}^{-\mathrm{i}kx - \mathrm{i}\alpha Y} \,\mathrm{d}k, \tag{A.1}$$

for $Y > 0$, where $\alpha(k) = \sqrt{(\omega - Mk)^2 - k^2}$ with $\mathrm{Im}(\alpha) < 0$ for $k \in \mathbb{R}$. Eq. (9a) for $\hat{p}_{\mathrm{dir}}$ is of this form with $Y = |y - y_s|$ and $f(k/\omega, \alpha/\omega) \equiv 1$, and Eq. (9b) for $\hat{p}_{\mathrm{refl}}$ is also of this form with $Y = y + y_s$ and $f(k/\omega, \alpha/\omega) \equiv \big[Z\alpha/\omega - (1 - Mk/\omega)^2\big]/\big[Z\alpha/\omega + (1 - Mk/\omega)^2\big]$.

AppendixA.1. Derivation of the steepest descent contour

We first look for saddle points in the integrand exponent $Q(k) = -\mathrm{i}kx - \mathrm{i}\alpha Y$. Differentiating gives

$$\frac{\partial Q}{\partial k} = -\mathrm{i}\left(x - \frac{Y}{\alpha}\big(\beta^2 k + M\omega\big)\right), \qquad \frac{\partial^2 Q}{\partial k^2} = \frac{\mathrm{i}Y\omega^2}{\alpha^3}, \tag{A.2}$$

where $\beta^2 = 1 - M^2$. Saddle points $k = k_s$ are given by $\partial Q/\partial k = 0$, which rearranges to give a quadratic equation for k_s with solutions

$$k_s = \frac{\omega}{\beta^2}\big(x/r - M\big) \qquad \Rightarrow \qquad \alpha_s = Y\omega/r \qquad \text{and} \qquad Q(k_s) = \frac{\mathrm{i}\omega}{\beta^2}\big(Mx - r\big), \tag{A.3}$$

where $r^2 = x^2 + \beta^2 Y^2$. (Note that, since $\mathrm{Im}(\omega) = -\varepsilon < 0$ and since the branch of α was chosen such that $\mathrm{Im}(\alpha) < 0$ for real k, the other root of the quadratic equation does not lead to a saddle point and is therefore discarded.) The steepest descent contour $k_{\mathrm{sd}}(q)$ for $q \in \mathbb{R}$ is then given by requiring

$$Q\big(k_{\mathrm{sd}}(q)\big) = Q(k_s) - q^2/2. \tag{A.4}$$

Inverting this gives the steepest descent contour as

$$k_{\mathrm{sd}}(q) = \frac{\omega}{\beta^2}\left(\frac{x}{r} - M\right) - \frac{\mathrm{i}xq^2}{2r^2} + \frac{Yq}{r^2}\sqrt{\mathrm{i}\omega r + \beta^2 q^2/4}, \tag{A.5a}$$

$$\alpha_{\mathrm{sd}}(q) = \frac{\omega Y}{r} - \frac{\mathrm{i}\beta^2 Y q^2}{2r^2} - \frac{xq}{r^2}\sqrt{\mathrm{i}\omega r + \beta^2 q^2/4}, \tag{A.5b}$$

$$\frac{\mathrm{d}k_{\mathrm{sd}}}{\mathrm{d}q} = \mathrm{i}\alpha_{\mathrm{sd}}(q)\big(\mathrm{i}\omega r + \beta^2 q^2/4\big)^{-1/2}, \tag{A.5c}$$

with the branch chosen such that $\mathrm{Re}(\sqrt{\mathrm{i}\omega r + \beta^2 q^2/4}) > 0$ so that the contour given by Eq. (A.5a) is traversed in the correct direction.

For large $|q|$ and real ω, Eq. (A.5a) shows that $\mathrm{Re}(-\mathrm{i}xk_{\mathrm{sd}}) = -x^2q^2/(2r^2) + O(1)$, and therefore for both the cases $x > 0$ and $x < 0$ deforming the integration contour onto the steepest descent contour moves both ends of the integration contour into sectors of the k-plane where the integrand is exponentially small. Moreover, from Eq. (A.5b) it can be shown that α_{sd} is never zero for real q, so that poles of the integrand due to the $1/\alpha$ factor are not crossed when deforming the contour. Deforming the integration contour onto the steepest descent contour is therefore possible provided attention is paid to any poles of $f(k/\omega, \alpha/\omega)$, and therefore I is given by the steepest descent integral

$$\begin{aligned} I(x, Y) = {} & \frac{\mathrm{i}\mathrm{e}^{-\mathrm{i}\omega r(1 - Mx/r)/\beta^2}}{4\pi}\int_{-\infty}^{\infty} f\left(\frac{k_{\mathrm{sd}}(q)}{\omega}, \frac{\alpha_{\mathrm{sd}}(q)}{\omega}\right)\frac{\omega - Mk_{\mathrm{sd}}(q)}{\sqrt{\mathrm{i}\omega r + \beta^2 q^2/4}}\mathrm{e}^{-q^2/2}\,\mathrm{d}q \\ & - \sum_{k \in \mathcal{K}_-}\frac{\mathrm{i}(\omega - Mk)}{2\alpha(k)}R_k\mathrm{e}^{-\mathrm{i}kx - \mathrm{i}\alpha(k)Y} + \sum_{k \in \mathcal{K}_+}\frac{\mathrm{i}(\omega - Mk)}{2\alpha(k)}R_k\mathrm{e}^{-\mathrm{i}kx - \mathrm{i}\alpha(k)Y}, \end{aligned} \tag{A.6}$$

where $\mathcal{K}_+$ and $\mathcal{K}_-$ are the poles of $f(k/\omega, \alpha/\omega)$ lying either in the upper-half k-plane below the steepest descent contour ($\mathcal{K}_+$) or in the lower-half k-plane above the steepest descent contour ($\mathcal{K}_-$), and R_k are their residues. Eq. (A.6) is easily numerically tractable due to the $\mathrm{e}^{-q^2/2}$ term and lack of oscillatory behaviour in the exponential due to the choice of contour. Moreover, since the steepest descent contour was chosen, asymptotic analysis in the far field $r \gg 1$ is possible.

AppendixA.2. Derivation of far-field asymptotics

We are interested here in the behaviour of Eq. (A.6) in the limit $r \gg 1$. Since the contour chosen is exactly the steepest descent contour, with the only saddle point crossed at $q = 0$, the asymptotics are easily found using the Method of Steepest Descents by expanding the integrand about $q = 0$ [see, e.g. 46, for details]:

$$\begin{aligned} I(x,Y) = \sqrt{\frac{\omega}{8\pi r}}\frac{1-Mx/r}{\beta^2}\exp\left\{-\mathrm{i}\omega r\frac{1-Mx/r}{\beta^2}+\mathrm{i}\pi/4\right\} f\left(\frac{1}{\beta^2}\left(\frac{x}{r}-M\right),\frac{Y}{r}\right)\left(1+O\left(\frac{1}{\omega r}\right)\right) \\ -\sum_{k\in\mathcal{K}_-}\frac{\mathrm{i}(\omega-Mk)}{2\alpha(k)}R_k\mathrm{e}^{-\mathrm{i}kx-\mathrm{i}\alpha(k)Y}+\sum_{k\in\mathcal{K}_+}\frac{\mathrm{i}(\omega-Mk)}{2\alpha(k)}R_k\mathrm{e}^{-\mathrm{i}kx-\mathrm{i}\alpha(k)Y}. \end{aligned} \tag{A.7}$$

AppendixB. $\mathcal{R}(x)$ for a nonlocally reacting impedance

If the impedance $Z(k,\omega)$ is a function of the wavenumber k as well as the frequency ω, then the procedure described in §6 to calculate the generalized reflection coefficient $\mathcal{R}(x)$ must be altered. While the procedure given here is valid for any impedance for which $k/Z(k,\omega) \to 0$ as $|k| \to \infty$, for definiteness here we consider an elastic tension T along the impedance surface such that $Z(k,\omega) = Z_{\mathrm{loc}}(\omega) - \mathrm{i}Tk^2/\omega$, where Z_{loc} is a locally reacting impedance. In this case,

$$\mathcal{R}(x) = \delta(x) + \underbrace{\frac{-1}{2\pi}\int_{-\infty}^{\infty}\frac{2(\omega-Mk)^2}{\alpha\omega Z+(\omega-Mk)^2}\mathrm{e}^{-\mathrm{i}kx}\,\mathrm{d}k}_{\hat{I}_0(x)} \tag{B.1a}$$

$$\begin{aligned} &= \delta(x) - \frac{\mathrm{i}M^2}{T\beta}\mathrm{e}^{\mathrm{i}\omega Mx/\beta^2}H_0^{(2)}\big(\omega|x|/\beta^2\big) \\ &\quad + \underbrace{\frac{1}{2\pi}\int_{-\infty}^{\infty}\frac{2\omega^2T\alpha-4Mk\omega T\alpha-2\mathrm{i}M^2\alpha\omega Z_{\mathrm{loc}}-2\mathrm{i}M^2(\omega-Mk)^2}{T\alpha\big[\alpha\omega Z+(\omega-Mk)^2\big]}\mathrm{e}^{-\mathrm{i}kx}\,\mathrm{d}k}_{\hat{I}_1(x)}, \end{aligned} \tag{B.1b}$$

where again the integrand of $\hat{I}_0$ in Eq. (B.1a) has no pole at $\alpha = 0$ but is $O(1/|k|)$ as $|k| \to \infty$, leading to a logarithmic singularity of $\hat{I}_0$ at $x = 0$, while $\hat{I}_1$ in Eq. (B.1b) is $O(1/|k|^2)$ as $|k| \to \infty$, so is expected to be regular at $x = 0$, but introduces a pole at $\alpha = 0$.

Note that, in this case, the line of line sources consists of an equal source ($\delta(x)$), as if for a rigid surface ($Z = \infty$), plus a correction to account for the impedance. This contrasts with the locally reacting impedance, for which the line of line sources consists of an equal but opposite source ($-\delta(x)$), as if for a pressure release surface ($Z = 0$), plus a correction to account for the impedance.

References

[1] E. J. Brambley, G. Gabard, Time Domain Simulations using the Modified Myers Boundary Condition, AIAA Paper 2013-2218, 2013.

[2] T. F. W. Embleton, J. E. Piercy, N. Olson, Outdoor Sound Propagation over Ground of Finite Impedance, J. Acoust. Soc. Am. 59 (2) (1976) 267–277.

[3] P. Mungur, H. E. Plumblee, Propagation and Attenuation of Sound in a Soft-walled Annular Duct containing a Sheared Flow, NASA SP-207, 305–327, 1969.

[4] S. W. Rienstra, A Classification of Duct Modes based on Surface Waves, Wave Motion 37 (2003) 119–135.

[5] P. M. Morse, R. H. Bolt, Sound Waves in Rooms, Revs. Modern Phys. 16 (2) (1944) 69–150.

[6] D. I. Paul, Acoustic Radiation from a Point Source in the Presence of Two Media, J. Acoust. Soc. Am. 29 (10) (1957) 1102–1109.

[7] K. Attenborough, S. I. Hayek, J. M. Lawther, Propagation of Sound above a Porous Half-Space, J. Acoust. Soc. Am. 68 (5) (1980) 1493–1501.

[8] S.-I. Thomasson, A Powerful Asymptotic Solution for Sound Propagation above an Impedance Boundary, Acoustica 45 (1980) 122–125.

[9] A. D. Rawlins, The Field of a Spherical Wave Reflected from a Plane Absorbent Surface Expressed in Terms of Infinite Series of Legendre Polynomials, J. Sound Vib. 89 (3) (1983) 359–363.
[10] G. Taraldsen, The Complex Image Method, Wave Motion 43 (2005) 91–97.
[11] S. N. Chandler-Wilde, D. C. Hothersall, Sound Propagation Above an Inhomogeneous Impedance Plane, J. Sound Vib. 98 (4) (1985) 475–491.
[12] S. N. Chandler-Wilde, D. C. Hothersall, Efficient Calculation of the Green Function for Acoustic Propagation above a Homogeneous Impedance Plane, J. Sound Vib. 180 (5) (1995) 705–724.
[13] S. N. Chandler-Wilde, D. C. Hothersall, A Uniformly Valid Far Field Asymptotic Expansion of the Green Function for Two-Dimensional Propagation Above a Homogeneous Impedance Plane, J. Sound Vib. 182 (5) (1995) 665–675.
[14] F. P. Mechel, A Line Source Above a Plane Absorber, Acustica united with Acta Acustica 86 (2) (2000) 203–215.
[15] E. J. Brambley, Surface Modes in Sheared Boundary Layers over Impedance Linings, J. Sound Vib. 332 (2013) 3750–3767, doi:10.1016/j.jsv.2013.02.028.
[16] S. W. Rienstra, B. J. Tester, An Analytic Green's Function for a Lined Circular Duct Containing Uniform Mean Flow, J. Sound Vib. 317 (2008) 994–1016.
[17] E. J. Brambley, N. Peake, Classification of Aeroacoustically Relevant Surface Modes in Cylindrical Lined Ducts, Wave Motion 43 (2006) 301–310.
[18] D. G. Crighton, The 1988 Rayleigh Medal Lecture: Fluid Loading — the Interaction between Sound and Vibration, J. Sound Vib. 133 (1989) 1–27.
[19] C. Richter, Liner Impedance Modeling in the Time Domain with Flow, Ph.D. thesis, Technische Universität Berlin, 2009.
[20] S. W. Rienstra, Sound Transmission in Slowly Varying Circular and Annular Lined Ducts with Flow, J. Fluid Mech. 380 (1999) 279–296.
[21] S. W. Rienstra, W. Eversman, A Numerical Comparison Between the Multiple-Scales and Finite-Element Solution for Sound Propagation in Lined Flow Ducts, J. Fluid Mech. 437 (2001) 367–384.
[22] S. W. Rienstra, Sound Propagation in Slowly Varying Lined Flow Ducts of Arbitrary Cross-Section, J. Fluid Mech. 495 (2003) 157–173.
[23] N. C. Ovenden, S. W. Rienstra, Mode-Matching Strategies in Slowly Varying Engine Ducts, AIAA J. 42 (9) (2004) 1832–1840.
[24] E. J. Brambley, N. Peake, Sound Transmission in Strongly Curved Slowly Varying Cylindrical Ducts with Flow, J. Fluid Mech. 596 (2008) 387–412.
[25] M. G. Jones, W. R. Watson, T. L. Parrott, Benchmark Data for Evaluation of Aeroacoustic Propagation Codes with Grazing Flow, AIAA Paper 2005-2853, 2005.
[26] Y. Özyörük, L. N. Long, Time-Domain Calculation of Sound Propagation in Lined Ducts with Sheared Flows, AIAA J. 38 (5) (2000) 768–773.
[27] M. O. Burak, M. Billson, L.-E. Eriksson, S. Baralon, Validation of a Time & Frequency Domain Grazing Flow Acoustic Liner Model, AIAA Paper 2008-2929, 2008.
[28] Y. Renou, Y. Aurégan, Failure of the Ingard–Myers Boundary Condition for a Lined Duct: An Experimental Investigation, J. Acoust. Soc. Am. 130 (2011) 52–60, doi:10.1121/1.3586789.
[29] G. Gabard, A Comparison of Impedance Boundary Conditions for Flow Acoustics, J. Sound Vib. 332 (2013) 714–724, doi:10.1016/j.jsv.2012.10.014.
[30] Y. Özyörük, Numerical Prediction of Aft Radiation of Turbofan Tones through Exhaust Jets, J. Sound Vib. 325 (2009) 122–144.
[31] E. J. Brambley, A well-posed boundary condition for acoustic liners in straight ducts with flow, AIAA J. 49 (6) (2011) 1272–1282, doi:10.2514/1.J050723.
[32] Y. Aurégan, R. Starobinski, V. Pagneux, Influence of Grazing Flow and Dissipation Effects on the Acoustic Boundary Conditions at a Lined Wall, J. Acoust. Soc. Am. 109 (2001) 59–64.
[33] S. W. Rienstra, M. Darau, Boundary-Layer Thickness Effects of the Hydrodynamic Instability along an Impedance Wall, J. Fluid Mech. 671 (2011) 559–573.
[34] X. Wu, Generation of sound and instability waves due to unsteady suction and injection, J. Fluid Mech. 453 (2002) 289–313.
[35] T. Suzuki, S. K. Lele, Green's functions for a source in a boundary layer: direct waves, channelled waves and diffracted waves, J. Fluid Mech. 477 (2003) 129–173.
[36] E. J. Brambley, M. Darau, S. W. Rienstra, The Critical Layer in Linear-Shear Boundary Layers over Acoustic Linings, J. Fluid Mech. 710 (2012) 545–568, doi:10.1017/jfm.2012.376.
[37] E. J. Brambley, N. Peake, Stability and Acoustic Scattering in a Cylindrical Thin Shell Containing Compressible Mean Flow, J. Fluid Mech. 602 (2008) 403–426.
[38] M. K. Myers, On the Acoustic Boundary Condition in the Presence of Flow, J. Sound Vib. 71 (1980) 429–434.
[39] M. Abramowitz, I. A. Stegun, Handbook of Mathematical Functions, Dover, 9th edn., 1964.
[40] E. J. Brambley, Fundamental Problems with the Model of Uniform Flow over Acoustic Linings, J. Sound Vib. 322 (2009) 1026–1037.
[41] E. J. Brambley, N. Peake, Surface-Waves, Stability, and Scattering for a Lined Duct with Flow, AIAA Paper 2006-2688, 2006.
[42] K. M. Li, S. Taherzadeh, K. Attenborough, Sound Propagation from a Dipole Source near an Impedance Plane, J. Acoust. Soc. Am. 101 (6) (1997) 3343–3352.
[43] K. M. Li, S. Taherzadeh, The Sound Field of an Arbitrarily Oriented Quadrupole near Ground Surfaces, J. Acoust. Soc. Am. 102 (4) (1997) 2050–2057.

[44] W. Koch, Radiation of Sound from a Two-Dimensional Acoustically Lined Duct, J. Sound Vib. 55 (2) (1977) 255–274.
[45] S. W. Rienstra, Acoustic Scattering at a Hard–Soft Lining Transition in a Flow Duct, J. Eng. Math. 59 (2007) 451–475.
[46] E. J. Hinch, Perturbation Methods, chap. 3.3, Cambridge, 1991.